

Scalar Dispersion from Wall-Mounted Cylinders at Large Reynolds Number: Plume Transitions and Regime Classification

Kofi Agyemang Amankwah¹, Juan Carlos Cuevas Bautista¹, Theresa Oehmke¹, Christopher M. White^{1*}, Lukasz Zielinski², Gocha Chochua², Andrew Speck²

¹Department of Mechanical Engineering, University of New Hampshire, Durham, NH 03824, USA

²Schlumberger-Doll Research, One Hampshire St, Cambridge, MA 02139, USA

Abstract

This study presents a comprehensive experimental investigation of scalar dispersion from the free end of wall-mounted cylindrical obstacles immersed in a large-Reynolds-number turbulent boundary layer. A key focus is the characterization of transition behavior between distinct dispersion regimes: elevated plumes (EP), ground-level plumes (GLP), and ground-level sources (GLS). Experiments systematically vary the primary and secondary aspect ratios (AR_1 , AR_2) and the velocity ratio (r) to explore their effects on the evolution of scalar plumes. Plume classification is governed by the non-dimensional parameter \tilde{h}_s/δ_{cz} , which quantifies the progressive interaction between the plume and the ground. Here, \tilde{h}_s denotes the effective source height and δ_{cz} the vertical plume half-width. Detailed concentration measurements demonstrate that the EP–GLP–GLS transitions substantially modify both vertical and lateral dispersion characteristics. The measurements reveal systematic departures from classical dispersion-coefficient scaling. To assess the capability of existing models under these conditions, the experimentally determined dispersion coefficients are used to evaluate the Gaussian Dispersion Model (GDM) and a Wall Similarity Model (WSM). The GDM captures general trends but deviates in specific regimes, whereas the WSM offers improved representation under GLS conditions. The resulting dataset, grounded in systematic laboratory measurements, establishes a critical benchmark for validating numerical simulations and informing the development of next-generation predictive models. Finally, leveraging these results, a concise data-informed predictive framework is introduced that captures the EP–GLP–GLS transitions and provides first-order estimates of ground-level concentration across geometric and momentum-ratio parameter space.

1 Introduction

The ability to accurately predict scalar dispersion in turbulent boundary layer flows influenced by three-dimensional wall-flow effects is of critical importance across a wide range of natural processes and engineering and industrial applications. These include scalar transport around submerged obstacles in tidal flows, pollutant release from industrial facilities into the atmosphere, and the release of radionuclides, toxic chemicals, or airborne pathogens in urban environments. A fundamental challenge in accurately predicting scalar dispersion from a point source within the atmospheric boundary layer lies in the complex flow interactions induced by ground-based obstacles, typically situated at or downstream of the source and fully immersed within the boundary layer [15]. These obstacles generate inherently three-dimensional, unsteady flow fields characterized by concentrated

*Corresponding author: chris.white@unh.edu

regions of vorticity, complex vortex–vortex interactions, and high levels of fluctuating vorticity. Such coherent and incoherent turbulent flow structures can significantly influence, and in some cases intermittently dominate, scalar transport, leading to highly anisotropic and non-Gaussian dispersion behavior.

Owing to these complexities and their critical implications for environmental quality and public health, scalar dispersion downwind of wall-mounted obstacles immersed in boundary layer flow has long been, and remains, an active area of research [1–3, 11, 16, 17, 37]. These studies aim to advance our understanding of the underlying flow physics that govern scalar transport in such configurations, with the goal of developing more accurate predictive models for use in urban environments and complex industrial settings. Dispersion models used for regulatory compliance are based on Gaussian dispersion models (GDM) [5, 29]. The modeling and analysis then focus on predicting dispersion coefficients as a function of downwind distance, under a range of flow conditions, including the influence of wakes generated by ground-based structures. In contrast, simulation-based approaches, such as RANS, LES, and DNS, are more computationally intensive but can offer greater accuracy and insight [2, 3, 26, 28, 30, 38, 42].

In this study, scalar dispersion is investigated for releases from the free end of finite-height, wall-mounted cylinders immersed in a developing turbulent boundary layer at high Reynolds number. A near-neutrally buoyant mixture of 5% methane and 95% nitrogen by volume is injected at mean velocity u_s through a circular source of diameter d_s centered on the cylinder free end. The cylinder height h_s is held fixed, yielding $1.45 \leq \delta/h_s \leq 1.81$, where δ is the local boundary-layer thickness. Four release geometries are examined, characterized by primary aspect ratio $AR_1 \equiv h_s/d_o$ and secondary aspect ratio $AR_2 \equiv d_o/d_s$: $AR_1 = 11.47, 4.72, 1.3, 0.7$ and $AR_2 = 1.22, 2.96, 10.75, 19.95$. To the authors' knowledge, these experiments represent the highest boundary-layer Reynolds number ($\delta^+ \simeq 6,210$) and bluff-body Reynolds number ($Re_{d_o} \simeq 1.82 \times 10^5$) reported for wind-tunnel studies of scalar dispersion involving wall-mounted obstacles.

The primary objective is to quantify how three-dimensional wall-flow interactions govern EP–GLP–GLS plume transitions, which strongly influence ground-level exposure. In this context, the predictive performance of the Gaussian Dispersion Model (GDM) is assessed under transition conditions and compared against a Wall Similarity Model (WSM). The resulting high-Reynolds-number dataset provides validation material for numerical simulations and analytical dispersion models relevant to complex near-wall release scenarios. Finally, leveraging these results, a concise data-informed predictive model is introduced that discriminates EP–GLP–GLS transitions and provides first-order estimates of ground-level concentration across geometric and momentum-ratio parameter space.

2 Scalar dispersion models

2.1 Gaussian dispersion model

The Gaussian dispersion model underpins most open-air pollutant models employed by regulatory agencies, including the U.S. EPA's AERMOD [5]. While the primary advantage of GDM lies in its simplicity and tractability, this comes at the cost of generalized assumptions that can be violated in complex wall-bounded flows [40]. Despite these limitations, the GDM often performs well in practice when empirically calibrated parameters are employed [6, 10, 33].

The standard GDM formulation of Pasquill [21] to compute steady concentration $C(x, y, z)$ is recast into a form that is more convenient for describing and interpreting the EP–GLP–GLS

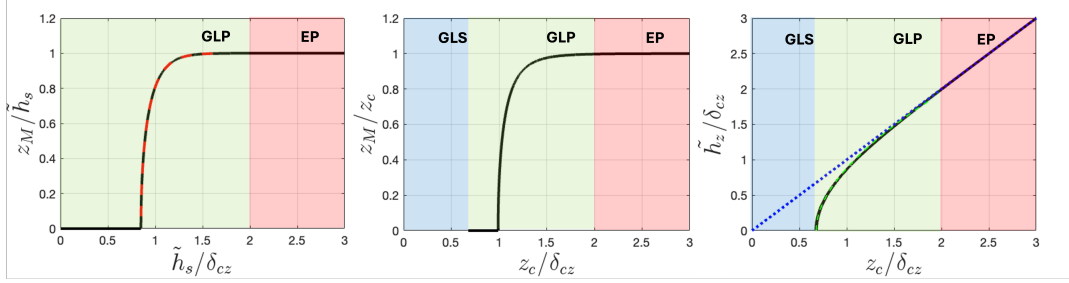


Figure 1: (left) The normalized vertical location of peak concentration z_M/\tilde{h}_s versus \tilde{h}_s/δ_{cz} (black curve). The red dashed line is a derived analytical solution $\tilde{h}_s/\delta_{cz} = \sqrt{\tanh^{-1}(\hat{z}_M)/(2 \ln(2) \hat{z}_M)}$ valid for $0 < z_M/\tilde{h}_s < 1$, where $\hat{z}_M = z_M/\tilde{h}_s$. (middle) z_M/z_c versus z_c/δ_{cz} . (right) \tilde{h}_s/δ_{cz} versus z_c/δ_{cz} . The green dotted line is the fit $\tilde{h}_s/\delta_{cz} = 1.68(z_c/\delta_{cz} - \chi_{GLS})^{0.66} + 0.05(z_c/\delta_{cz} - \chi_{GLS})$, valid for $0 < z_c/\tilde{h}_s < 1.55$. The blue dotted line is $\tilde{h}_s/\delta_{cz} = z_c/\delta_{cz}$ shown for reference.

transition behavior:

$$C(x, y, z) = \frac{Q \ln(2)}{\pi U \delta_{cy} \delta_{cz}} \exp \left[-\ln(2) \frac{(y - y_s)^2}{\delta_{cy}^2} \right] \times \left\{ \exp \left[-\ln(2) \frac{(z - \tilde{h}_s)^2}{\delta_{cz}^2} \right] \left[1 + \exp \left(-\ln(2) \frac{4z\tilde{h}_s}{\delta_{cz}^2} \right) \right] \right\}, \quad (1)$$

for a source located at $(0, y_s, h_s)$ with emission rate Q in the presence of a wall at $z = 0$. Here, δ_{cy} and δ_{cz} denote the plume half-widths at half-maximum (HWHM), U is the steady downwind velocity, and $\tilde{h}_s = h_s + \Delta h_s$ is the effective source height accounting for plume rise or fall due to buoyancy or source effects. The image-source term ($\exp[-\ln(2) 4z\tilde{h}_s/\delta_{cz}^2]$) enforces the boundary condition $\partial C/\partial z|_{z=0} = 0$.

The parameter that distinguishes EP, GLP, and GLS is \tilde{h}_s/δ_{cz} . Plume classification metrics that are height-dependent but independent of other release-geometry parameters— z_M/\tilde{h}_s , z_c/δ_{cz} , and their mapping—are summarized in figure 1, where z_M denotes the peak-concentration height and z_c the plume centroid. EPs interact weakly with the wall and are categorized by $\tilde{h}_s/\delta_{cz} \geq 2$. GLPs are categorized by $0 < \tilde{h}_s/\delta_{cz} < 2$, with the image-source contribution increasing as \tilde{h}_s/δ_{cz} decreases. At $\tilde{h}_s/\delta_{cz} = 0.85$, the peak concentration shifts to the wall, signifying a transition from dominance by the real source to dominance by the combined real-image source. The GLS regime is categorized by $\tilde{h}_s/\delta_{cz} = 0$ and, as derived from (1) or more generally from (2), $(z_c/\delta_{cz})_{GLS} = B/(\ln 2)^{1/s} \approx 0.68$, where $B(s) = \Gamma(2/s)/\Gamma(1/s)$, Γ denotes the gamma function, and $s = 2$. Herein, $\chi_{GLS} \equiv (z_c/\delta_{cz})_{GLS}$.

Direct measurement of \tilde{h}_s within the GLP regime is not feasible (here $\tilde{h}_s \neq z_c$; for example, in a GLS configuration $\tilde{h}_s = 0$ while $z_c > 0$). Instead, the plume centroid height z_c provides a measurable surrogate. The right-hand panel of figure 1 shows the relationship between z_c/δ_{cz} and \tilde{h}_s/δ_{cz} . The two quantities coincide closely until $\tilde{h}_s/\delta_{cz} \lesssim 1.5$. The green dotted line denotes the empirical fit used to map z_c/δ_{cz} to \tilde{h}_s/δ_{cz} .

2.2 Wall similarity models

Serving as a comparator to the GDM, the WSM is examined in the context of plumes transitioning from a GLP to a GLS. WSM incorporates height-dependent mean velocity and diffusivity, e.g. $U(z) = u_1 z^m$, $D_z(z) = K_1 z^n$ [8, 39]. For a GLS, the WSM crosswind y -integrated profile $C' = \int C dy$

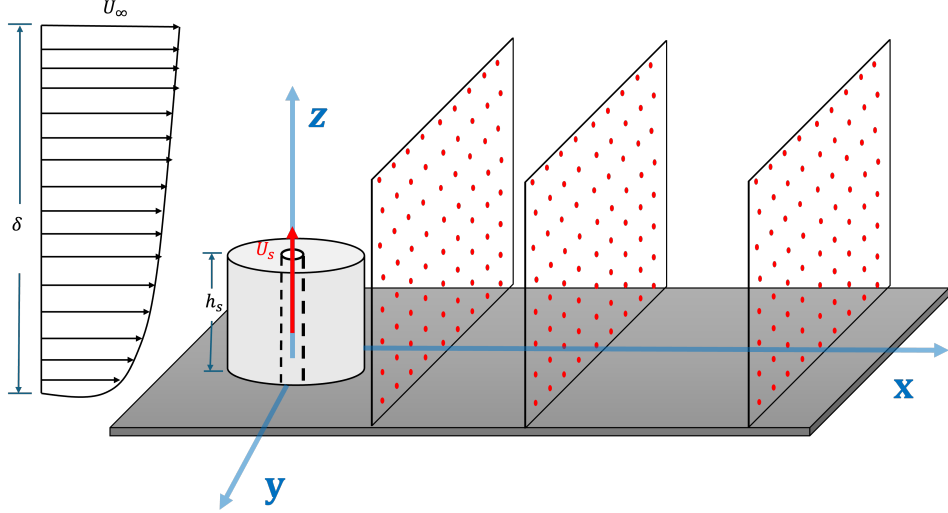


Figure 2: Schematic of the scalar release setup (GEOM2–GEOM4 shown). The inner dashed cylinder is the source (GEOM1). Measurement planes P_1, P_2, P_3 capture plume development.

has the normalized form

$$\frac{C'(x, z)}{C'_M} = \exp \left[-\ln 2 \left(\frac{z}{\delta_{cz}} \right)^s \right], \quad (2)$$

with shape factor $s = 2 + m - n$; $s = 2$ recovers a Gaussian distribution. Field and laboratory studies generally find $1.5 \lesssim s \lesssim 1.7$: Robins [24] reported $s = 1.7$ in urban flows; Fackrell and Robins [7] reported $s = 1.5$ in zero pressure gradient (ZPG) rough-wall boundary layer; Lim and Vanderwel [12] reported $s = 1.5$ in ZPG smooth-wall boundary layer. The non-Gaussian behavior implies that for $s < 2$, $\chi_{\text{GLS,WSM}} > \chi_{\text{GLS,GDM}}$; for example, when $s = 1.5$, $\chi_{\text{GLS,WSM}} \approx 0.84$. Thus, defining the GLP–GLS transition solely by χ_{GLS} is not without uncertainty.

3 Experiments

3.1 Facility and scalar release geometry

Experiments are performed in the UNH Flow Physics Facility (FPF), a ZPG wind tunnel with $2.8 \times 6 \text{ m}^2$ cross-section and 72 m fetch; see Vincenti et al. [41]. The setup is shown in figure 2. Four wall-mounted cylinders share a common internal source (GEOM1) and differ by outer diameter. Geometry details and aspect ratios $AR_1 = h_s/d_o$, $AR_2 = d_o/d_s$ are in Table 1. GEOM1 consists of a smooth-walled polyvinyl chloride (PVC) cylinder pipe with an inner diameter of $d_s = 20.375 \pm 0.056 \text{ mm}$ and an outer diameter of $d_o = 24.85 \pm 0.055 \text{ mm}$. The ends are precisely machined to be flat and sharp-edged. This pipe is vertically inserted into the FPF test section at $x_s = 27.54 \text{ m}$ through an aperture in the test section floor. The three additional release geometries are constructed using larger-diameter PVC pipes, also machined with flat surfaces and sharp edges. A smooth free end surface is machined to tolerance from 19.05 mm-thick high-density polyethylene (HDPE) and press-fitted into the inner diameter of each pipe, flush with its top edge. A central circular orifice of diameter $25.03 \pm 0.027 \text{ mm}$ is milled through the HDPE free end surface. These larger PVC assemblies are then mounted over GEOM1 such that the free end of the inner GEOM1 pipe is flush with the outer HDPE free end surface, thereby forming composite release configurations for GEOM2, GEOM3, and GEOM4.

	d_s (mm)	d_o (mm)	h_s (mm)	AR_1 (h_s/d_o)	AR_2 (d_o/d_s)
GEOM1	20.375	24.85	285	11.47	1.22
GEOM2	20.375	60.33	285	4.72	2.96
GEOM3	20.375	219.1	285	1.30	10.75
GEOM4	20.375	406.4	285	0.70	19.95

Table 1: Geometrical dimensions and AR_1 and AR_2 of the four release geometries.

$\simeq U_\infty$ (m s^{-1})	$\simeq u_\tau$ (m s^{-1})	$\simeq \delta_{99}$ (m)	$\simeq \delta^+$	$\simeq \delta/h_s$	$\simeq Re_{d_o} \times 10^4$ GEOM1/GEOM2/GEOM3/GEOM4
2.24	0.084	0.515	2800	1.81	0.371 / 0.901 / 3.27 / 6.07
4.48	0.163	0.444	4820	1.56	0.742 / 1.80 / 6.54 / 12.1
6.72	0.225	0.413	6210	1.45	1.11 / 2.70 / 9.82 / 18.2

Table 2: Boundary layer parameters at $x_s = 27.54$ m and Reynolds number of cylinders.

3.2 Approach flow

The approach flow is a developing ZPG turbulent boundary layer. Tests use $U_\infty \simeq 2.24, 4.48, 6.72 \text{ m s}^{-1}$, giving $\delta/h_s \simeq 1.81, 1.56, 1.45$. Boundary layer parameters and $Re_{d_o} = U_\infty d_o / \nu$ are in Table 2. Mean and variance profiles confirm canonical behavior; the cylinder free end lies within the outer layer, and the upper bound of the logarithmic region is approximately $0.2 - 0.3h_s$.

3.3 Scalar release

A premixed gas (5% methane / 95% nitrogen by volume) is injected through GEOM1 at fixed $u_s = 1.03 \pm 3\% \text{ m s}^{-1}$ in jet-in-crossflow configuration [4, 32]. The gas is supplied from a pressure-regulated compressed-gas cylinder. An in-line flow meter and insertion thermocouple measure volumetric flow rate and temperature. The effective velocity ratio r is the square root of the momentum-flux ratio

$$r = \left(\frac{\rho_s u_s^2}{\rho_\infty U_\infty^2} \right)^{1/2}, \quad (3)$$

and takes values $r \simeq 0.46, 0.23, 0.16$. The analysis is restricted to low-momentum releases ($r < r_c$) that confine the jet to the roof-wake boundary, with $r_c > 1.5$ reported previously [9].

3.4 Scalar concentration measurements

Methane concentration is measured with an *Aeris Technologies MIRA Ultra LDS* at 1 Hz via a 3.175 mm sampling probe on a two-axis traverse. Planes at $x \simeq 0.64, 1.66, 4.19$ m ($P1, P2, P3$) are scanned with ~ 100 points per plane. Measurement grids vary between experimental runs to accommodate differences in plume spread, with spacing ranging from 40 to 70 mm. Each measurement point is sampled for 30 s, with the duration constrained by the volume of the methane–nitrogen gas cylinder and the prescribed volumetric flow rate. A complete two-dimensional planar scan typically requires 2–3 h of continuous operation. Convergence testing is performed using 10-min samples at selected locations (Appendix A.1).

	GEOM1	GEOM2	GEOM3	GEOM4
	+	-	\times	
$\simeq U_\infty$ (m s^{-1})	$\simeq r$	$P1$ ($x_1/h_s \simeq 2.24$)	$P2$ ($x_2/h_s \simeq 5.82$)	$P3$ ($x_3/h_s \simeq 14.70$)
2.24	0.46 (—)	●	■	▲
4.48	0.23 (—)	●	■	▲
6.72	0.16 (—)	●	■	▲

Table 3: Data Symbols.

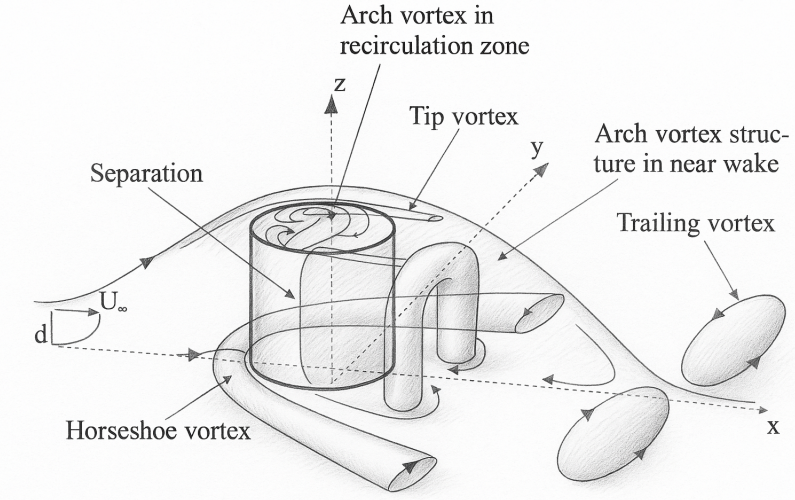


Figure 3: Schematic of time-averaged flow over a finite-height circular cylinder (adapted from [34]).

3.5 Scalar visualization

Smoke visualization is employed to qualitatively examine scalar dispersion near the cylinder free end and to track the initial trajectory of the injected scalar plume in the near field. A mixture of smoke and air is generated by combining the output of a centrifugal air blower with the discharge from a *ROSCO* fog machine in a large-volume plenum. This smoke-laden air is then routed to the release source and injected into the wind tunnel test section at $u_s = 1.03 \pm 3\% \text{ m s}^{-1}$. A *PCO Sensicam QE* records 289 images at 1 Hz (1376×1040 , 12-bit). Ensemble averages provide qualitative near-source plume structure.

4 The flow field of vertical wall-mounted cylinders

Finite-height cylinders in boundary layers produce rich three-dimensional flows with horseshoe vortices, tip vortices, arch vortices, and von Kármán shedding vortices [13, 20, 22, 23, 34, 35]. The topology depends on Re_{d_o} , AR_1 , and δ/h_s . A schematic is shown in figure 3.

A bifurcation with $AR_{1,\text{crit}}$ is often reported: for $AR_1 > AR_{1,\text{crit}}$, tip and Kármán vortices dominate; for $AR_1 < AR_{1,\text{crit}}$, a dominant arch vortex forms in the wake, and its interaction with Kármán and trailing-edge vortices governs the unsteady dynamics. Literature suggests $AR_{1,\text{crit}} \in [1, 7]$, with sensitivity to δ/h_s and configuration [34]. Dependencies include free-end reattachment, wake recirculation length, and arch vortex planform [20, 23, 27].

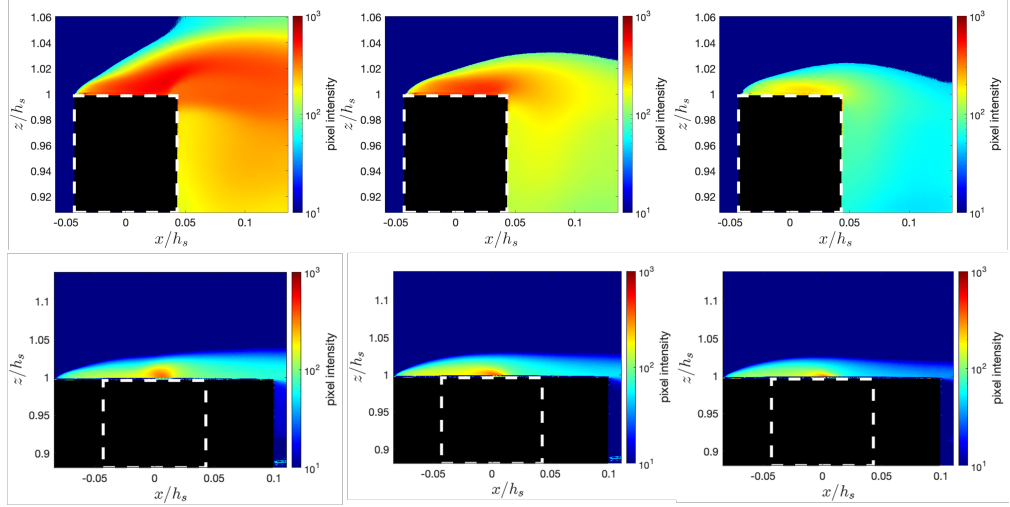


Figure 4: Ensemble-averaged smoke images near the source: GEOM1 (top), GEOM3 (bottom). Columns: $r \simeq 0.46, 0.23, 0.16$. Black box: outer geometry; dashed white box: source (GEOM1).

Rinoshika et al. [23] investigated $AR_1 = 1$ and observed that the tip vortex pair is centred at $y/d_o = \pm 0.5$ and extends to the ground due to strong downwash near $x/d_o = 3.5$. A W-shaped arch vortex was identified in the wake, with the vortex head at $y/d_o = 0$ and shoulders at $y/d_o = \pm 0.5$. The near-wake region exhibited a highly three-dimensional separated flow spanning most of the cylinder height, particularly from $y/d_o = \pm 0.2$. The combined effects of the W-shaped arch vortex and the horseshoe vortex on plume dispersion are discussed in §8.3.

5 Mean Scalar Fields

5.1 Source region

Ensemble-averaged smoke images near the free end ($0.9 \lesssim z/h_s \lesssim 1.2$) are shown in figure 4 for GEOM1 and GEOM3 across $r \simeq 0.46, 0.23, 0.16$. False-colour pixel intensity qualitatively represents scalar concentration indicating that dilution increases as r decreases. For GEOM1 the jet bends downwind and the centroid lowers with decreasing r . For GEOM3, the plume extends upwind toward the leading edge due to free-end recirculation. Instantaneous images show intermittent entrainment into the wake (GEOM1) and centroid flipping between downwind- and upwind-directed (GEOM3) at 1–2 Hz. For GEOM3, the upwind-directed centroid occurs more frequently, evidenced by the higher ensemble-averaged pixel intensity near the leading edge.

5.2 Near and far source region

Planar mean methane concentration fields are shown in figures 5–8. Rows: $r \simeq 0.46, 0.23, 0.16$. Columns: $x/h_s \simeq 2.24, 5.82, 14.70$. Dashed isoline marks $C = C_M/2$ (with C_M the peak concentration), providing a visual estimate of the plume half-width and overall dispersion extent. The colour map is $(C/C_o) \times 10^4$, where C_o is the source concentration. All cases show approximate lateral symmetry, stronger lateral than vertical spread, and a centroid below the source. GEOM1 behaves as an EP transitioning toward a GLP downstream; GEOM2 transitions EP–GLP–GLS across $P1–P3$; GEOM3 and GEOM4 exhibit near-source cavity-plume features and GLS-like behavior downstream, with stronger r -dependence for GEOM4.

The mean fields highlight the dominant role of the local flow structure at the release location in shaping scalar dispersion. Aspect ratio AR_1 and velocity ratio r are key parameters. For high aspect ratios ($AR_1 = 14.7, 4.72$), the plume is progressively forced downward by the free-end downwash, with the EP–GLP transition point depending on both AR_1 and r . For low aspect ratios ($AR_1 = 1.3, 0.7$), the scalar is drawn into the wake cavity, and the near-source fields resemble those of a bluff body cavity source. In the far-field, the plumes transition to GLS behavior.

6 Measurement of the dispersion coefficients

6.1 Direct measurements

Plume growth is quantified via: (i) half-width area A_{hw} ; (ii) area growth rate $\Phi = dA_{hw}/dx$; (iii) FWHM δ_{cz}, δ_{cy} measured through the centroid; and (iv) HWHM δ_{cz}, δ_{cy} from crosswind integration.

The variation of A_{hw} and Φ with downstream position x/h_s is shown in figure 9, where A_{hw} denotes the area enclosed by the iso-contour $C_M/2$, and $A_s = \pi d_s^2/4$ is the source area. GEOM1 exhibits a linear increase in A_{hw} , whereas GEOM2–GEOM4 display larger near-source values, reflecting enhanced lateral dispersion near the cylinder free end. GEOM2 shows an inflection at $x/h_s \approx 5.82$, coincident with the EP–GLP transition. GEOM3 remains approximately linear except at $r \simeq 0.46$, where Φ increases downstream of $x/h_s \approx 5.82$. GEOM4 exhibits the strongest r -dependence, highlighting the influence of AR_2 on plume development.

Full width at half maximum (FWHM) (Δ_{cz} and Δ_{cy}) are presented in figure 10. The suppression of vertical plume spread associated with the EP–GLP transition is evident in the behavior of Δ_{cz} . Notably, GLP and GLS plumes exhibit nearly constant vertical width, $\Delta_{cz} \approx 0.5h_s$, while the lateral extent remains significantly larger, $\Delta_{cy} \gg 2\Delta_{cz}$. Together, these measures provide a quantitative indicator of plume–ground interaction.

The downstream evolution of half-width at half-maximum (HWHM) δ_{cz}/d_s (dashed) and δ_{cy}/d_s (solid) is shown in figure 11. Crosswind integration suppresses the weak r -dependent variations observed in A_{hw}/A_s and the FWHM. For GEOM1, both δ_{cy} and δ_{cz} scale as $x^{1/2}$, with $\delta_{cy}/\delta_{cz} \approx 1.39 \pm 6\%$. GEOM2 also exhibits $\sim x^{1/2}$ scaling despite reduced vertical growth during the transition, indicating that FWHM remains a more reliable metric for identifying EP–GLP transitions. GEOM3 shows $\delta_{cy} \propto x^{-1}$ while $\delta_{cz}/h_s \approx 0.4$ remains nearly constant. GEOM4 transitions from $\delta_{cy} \propto x^{-1}$ at $r \simeq 0.46$ to $\delta_{cy} \propto x^{-0.6}$ at lower r , with δ_{cz}/h_s stabilizing in the range 0.4–0.5.

These results reflect complex interactions with vortex structures originating from the obstacle’s free end, sides, base, and shear layers. High- AR_1 release geometries are dominated by tip-vortex–induced downwash, leading to a faster EP–GLP transition and suppressed vertical spread. In contrast, low- AR_1 release geometries—which depend on both r and AR_2 —interact strongly with wake vortices, enhancing lateral mixing while suppressing vertical dispersion. The present findings are broadly consistent with the observations of Allwine et al. [1], who reported reduced vertical growth ($\sigma_z/h_s \approx 0.4$) and lateral-to-vertical spread ratios $\sigma_y/\sigma_z \approx 3$ for plumes released from wall-mounted structures under moderately stable stratification. Although arising from a different mechanism, a near-zero vertical growth rate, $d\delta_{cz}/dx \sim 0$, is also expected for plumes trapped beneath strong elevated-inversion caps in convective boundary layers [25].

In addition, the results highlight the importance of AR_2 , which appears to depend on the ratio δ_{cy}/d_o in the near-source region. For example, at $P1$, GEOM3 ($\delta_{cy}/d_o = 0.85 \pm 10\%$) exhibits strong interaction with wake vortices, whereas GEOM4 shows smaller values of $\delta_{cy}/d_o = 0.48, 0.41$, and 0.38 with decreasing r . The markedly faster plume spread for $r \simeq 0.46$ suggests that the plume half-width in the near-source region must exceed approximately $0.5d_o$ to experience strong coupling

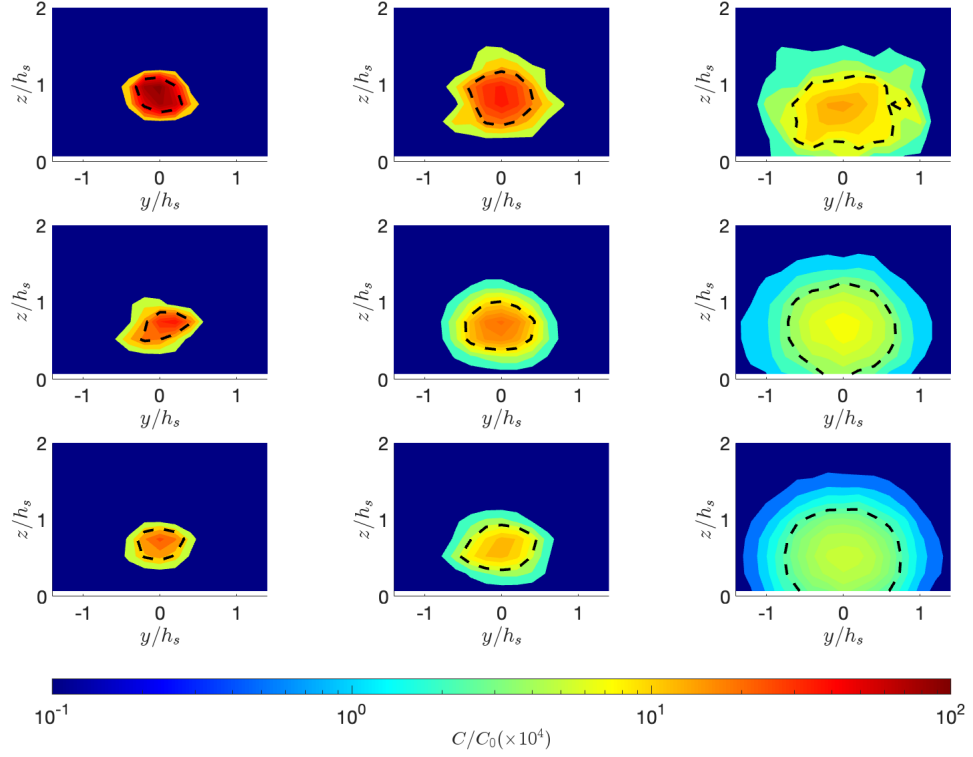


Figure 5: Mean concentration fields of GEOM1. Rows: $r \simeq 0.46, 0.23, 0.16$. Columns: $x/h_s \simeq 2.24, 5.82, 14.70$. Dashed isoline marks $C = C_M/2$. The colour map is $(C/C_o) \times 10^4$, where C_o is the source concentration.

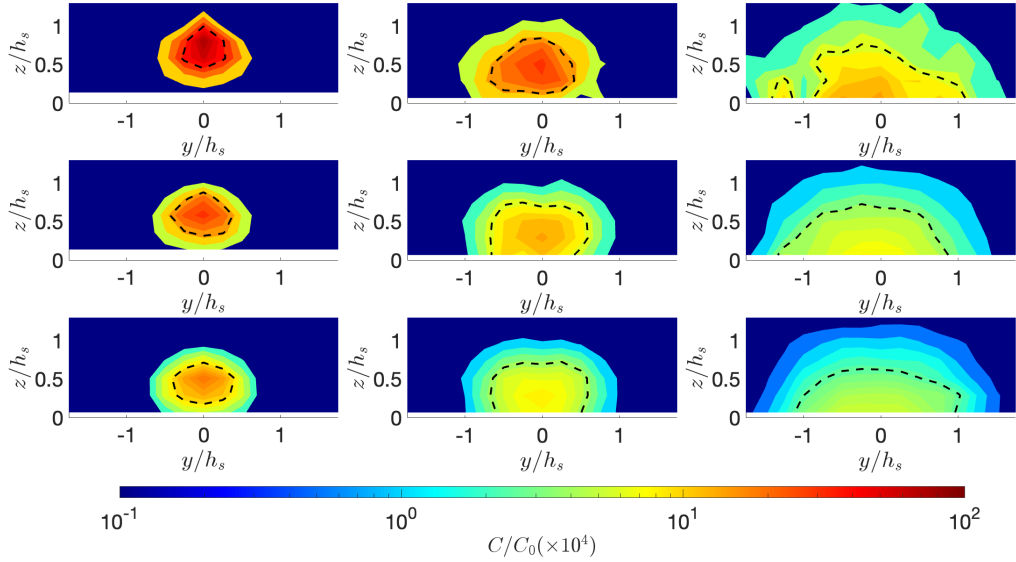


Figure 6: Mean concentration fields of GEOM2. The figure panel layout, colour map, and isoline are identical to those in figure 5.

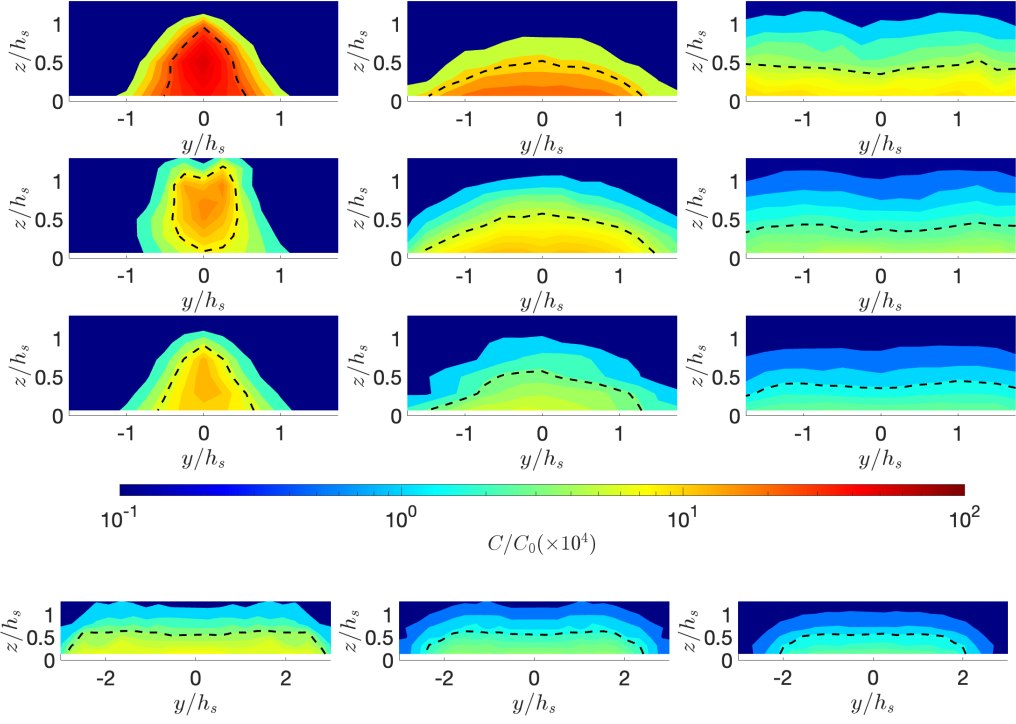


Figure 7: Mean concentration fields of GEOM3. The top 3×3 panel layout, colour map, and isoline are identical to those in figure 5. The bottom 1×3 panel shows a wider view at P_3 , with r decreasing from left to right.

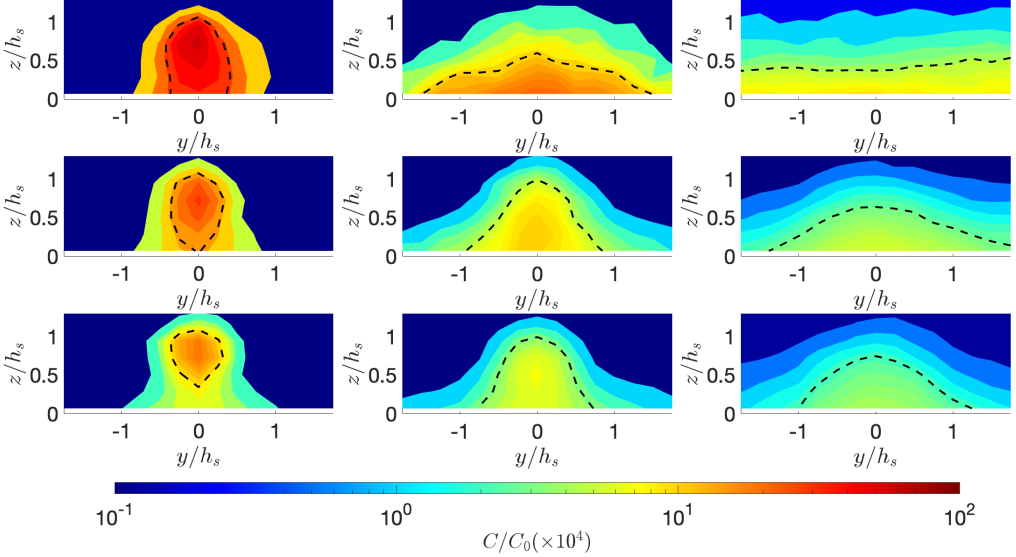


Figure 8: Mean concentration fields of GEOM4. The figure panel layout, colour map, and isoline are identical to those in figure 5. The wider view of $r1P3$ is not shown.

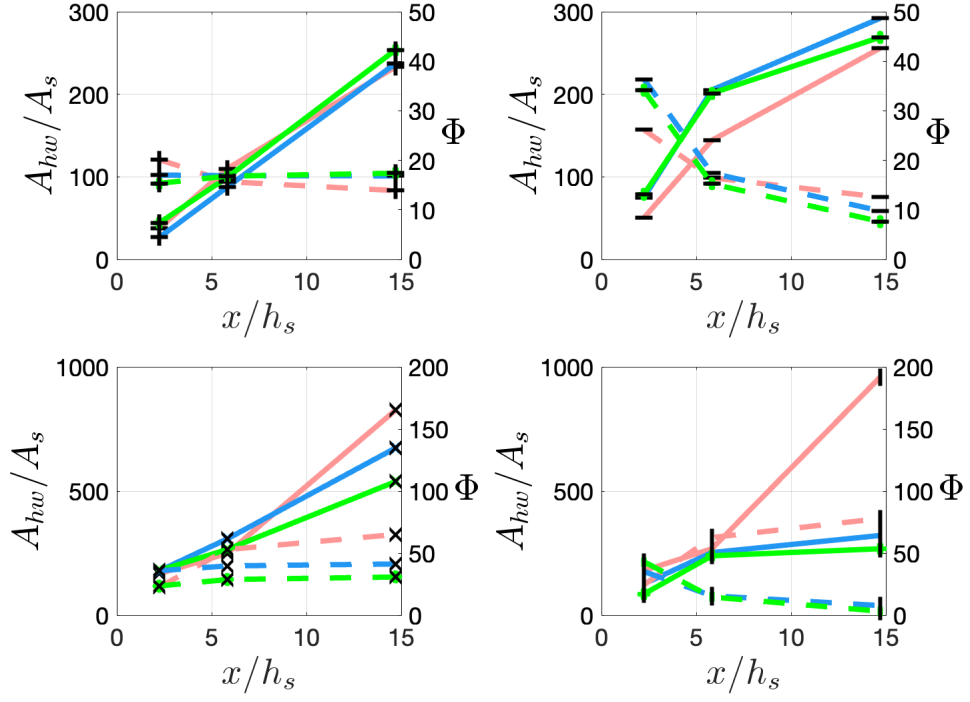


Figure 9: Normalized plume half-width area A_{hw}/A_s (solid, left axis) and spread rate Φ (dashed, right axis) versus x/h_s . Panels (left-to-right/top-to-bottom): GEOM1–GEOM4; colours denote r per Table 3.

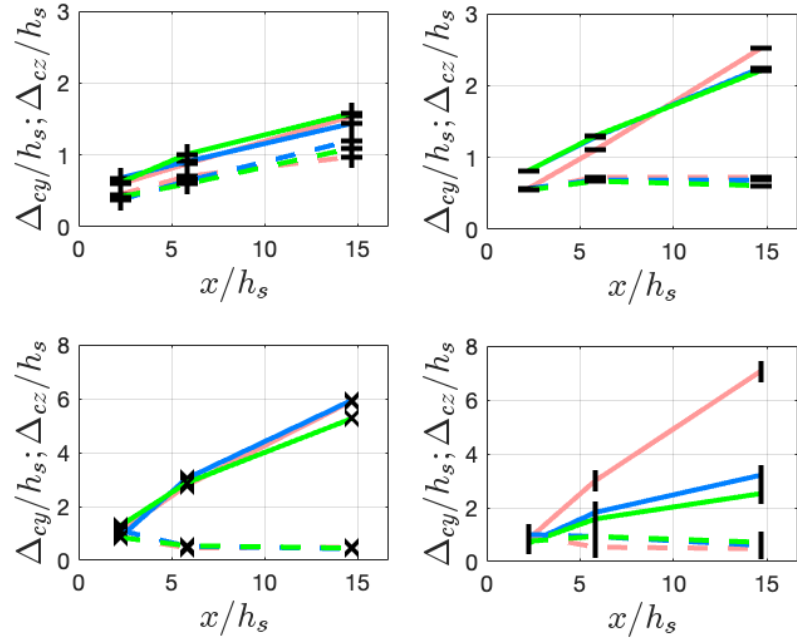


Figure 10: FWHM δ_{xy} (solid) and δ_{zz} (dashed) versus x/h_s . Panel layout and colours as in figure 9.

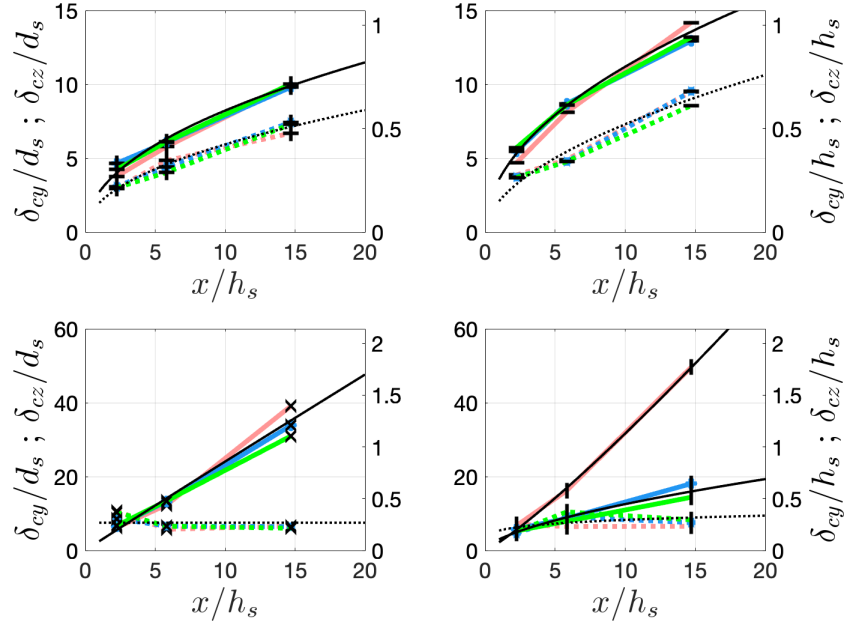


Figure 11: HWHM δ_{cy} (solid) and δ_{cz} (dashed) versus x/h_s . Black lines: power-law fits. Dual axes: left normalized by d_s ; right by h_s .

with wake vortices. For narrower plumes, wake vortices exert a correspondingly weaker influence on the dispersion process.

In summary, the standard GDM scaling, $(\delta_{cy}, \delta_{cz} \propto x^n)$ with $0.5 < n < 1$, does not hold for low-momentum, obstacle-influenced plumes. Accurate modeling requires the explicit inclusion of vortex-induced mixing and geometric effects, which can be captured empirically through correlations for δ_{cy} and δ_{cz} that depart from standard GDM behavior. The present results provide a foundation for developing such correlations.

6.2 Indirect measurements

From (1), the peak concentration is

$$C_M(x) = \frac{Q \ln(2)}{\pi U \delta_{cy} \delta_{cz}} \left\{ \exp \left[-\ln(2) \frac{(z_M - \tilde{h}_s)^2}{\delta_{cz}^2} \right] \left[1 + \exp \left(-\ln(2) \frac{4z_M \tilde{h}_s}{\delta_{cz}^2} \right) \right] \right\}. \quad (4)$$

The leading prefactor in (4) governs the primary decay of $C_M(x)$. The exponential terms introduce structure associated with the EP–GLP transition that can bias inferred decay rates toward slower values if the measurement domain spans the EP–GLP regime.

Profiles of normalized peak concentration, C_M/C_o , versus $x/(r d_s)$ are presented in figure 12. The solid red lines denote two-parameter power-law fits of the form $C_M/C_o = \beta(x/r d_s)^{-b}$, with fit parameters β and b listed in Table 4.

The sub-unity exponents ($b < 1$) indicate that the plume undergoes EP–GLP–GLS transitions and/or that the effective dispersion coefficients D_y , D_z , or advection velocity U vary with $x/r d_s$. Given $b \approx 1$, an estimate of $\sqrt{D_y D_z}$ can be obtained by neglecting the exponential terms in (4) and

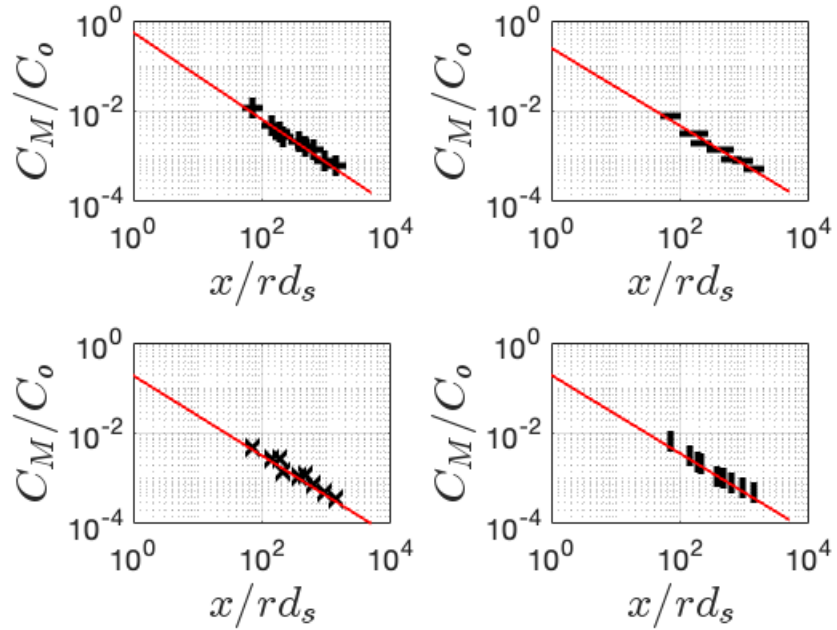


Figure 12: C_M/C_o versus x/rd_s : GEOM1 (top-left), GEOM2 (top-right), GEOM3 (bottom-left), GEOM4 (bottom-right). The solid red lines represent two parameter fits of the form $C_M/C_o = \beta(x/rd_s)^{-b}$.

Fit parameters	GEOM1	GEOM2	GEOM3	GEOM4
β	0.55	0.26	0.22	0.22
b	0.94	0.86	0.89	0.87

Table 4: Best-fit relations for the normalized peak concentration C_M/C_o .

r	GEOM1	GEOM2	GEOM3	GEOM4
0.46	5.19	10.97	12.30	12.30
0.23	10.14	21.45	25.35	25.35
0.16	15.60	32.91	38.90	38.90

Table 5: $\sqrt{D_y D_z} \times 10^{-3}$ (m² s⁻¹) computed from power-law fits.

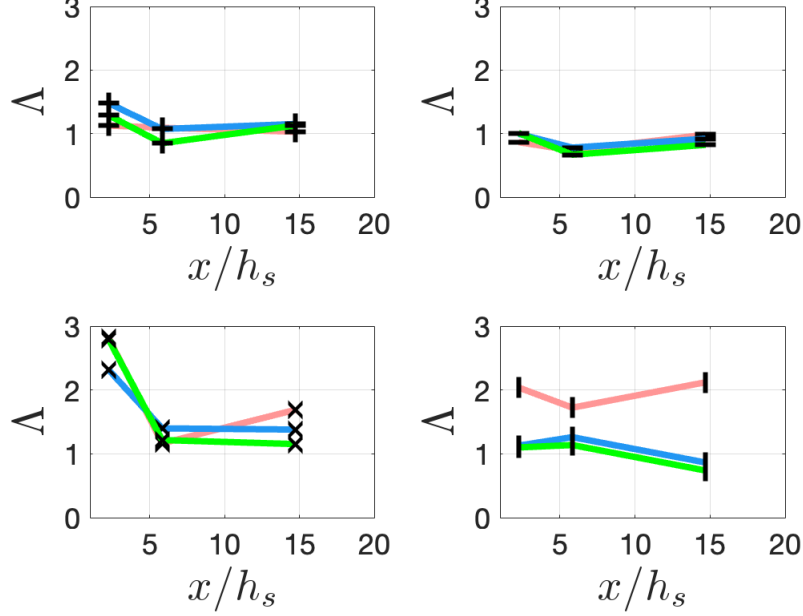


Figure 13: Ratio $\Lambda = (\delta_{cy}\delta_{cz})_m / (\delta_{cy}\delta_{cz})_f$ versus x/h_s for all cases. Panels (left-to-right/top-to-bottom): GEOM1–GEOM4; colours denote r per Table 3.

substituting $Q = C_o A_s u_s$:

$$\frac{C_M}{C_o} = \frac{A_s U_s}{4\pi r d_s \sqrt{D_y D_z}} \left(\frac{x}{r d_s} \right)^{-1} = \beta \left(\frac{x}{r d_s} \right)^{-1}, \quad (5)$$

where $A_s = \pi d_s^2 / 4$ and $r = u_s / U_\infty$ (neglecting small density differences between source gas and ambient air). Thus,

$$\beta = \frac{U_\infty d_s}{16 \sqrt{D_y D_z}}, \quad \text{or equivalently} \quad \sqrt{D_y D_z} = \frac{U_\infty d_s}{16 \beta}. \quad (6)$$

An indirect estimate of the effective diffusion coefficient product $\sqrt{D_y D_z}$ can be obtained from (6). This relation is analogous to a mixing-length model in which $D_y \sim u_y \lambda_y$ and $D_z \sim u_z \lambda_z$, with $u_y : u_z \propto U_\infty$ and $\lambda_y : \lambda_z \propto d_s$.

Assuming negligible x -dependence, the computed values of $\sqrt{D_y D_z}$ from Table 5 allow estimation of the product $\delta_{cy}\delta_{cz}$. These values are compared to directly measured half-width products in figure 13, using the ratio:

$$\Lambda = \frac{(\delta_{cy}\delta_{cz})_m}{(\delta_{cy}\delta_{cz})_f},$$

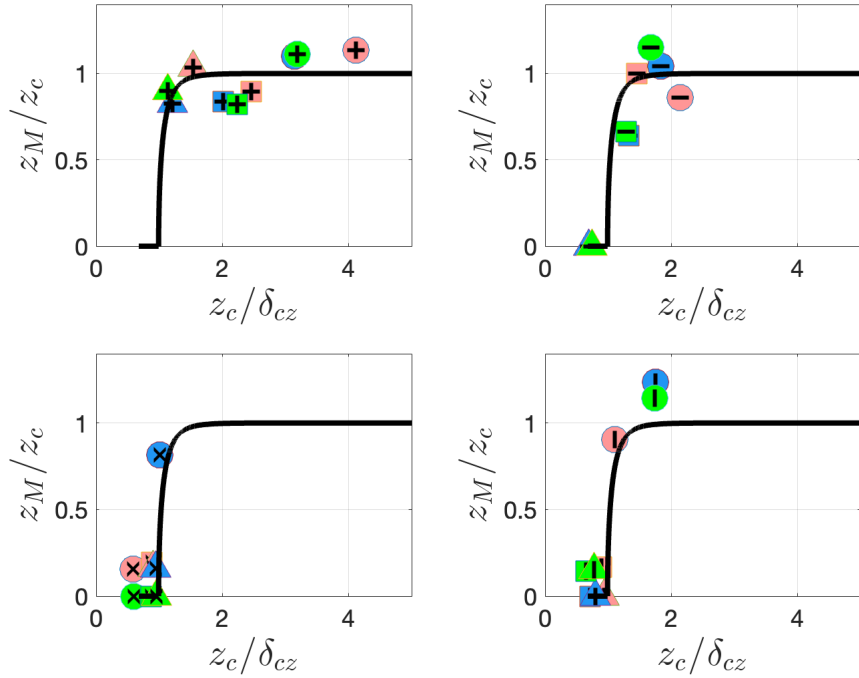


Figure 14: z_M/z_c versus z_c/δ_{cz} . The plot provides information on the plume type in each measurement plane. The solid black line in each panel is from figure 1. Panels (left-to-right/top-to-bottom): GEOM1–GEOM4; colours denote r and symbols denote P per Table 3.

where subscripts m and f denote measured and fitted values, respectively. For GEOM1 (EP) and GEOM2 (EP to GLS), the agreement is within $\pm 30\%$. For GEOM3 and GEOM4, particularly in the near-source region, the power-law fit underestimates the product by up to a factor of three.

This analysis demonstrates that the downstream decay of the peak concentration provides a valuable means for estimating the product $\sqrt{D_y D_z}$, and consequently $\delta_{cy} \delta_{cz}$. This approach is especially effective for elevated plumes, where deconvolution of the diffusion coefficients is feasible. For EPs, one can assume $\delta_{cy}/\delta_{cz} \simeq 1.4$ (see figure 11 discussion) to extract individual diffusion rates. For GLP/GLS, if the source height or diameter is known, the vertical half-width can be estimated as $\delta_{cz} \approx 0.45 h_s$ (or roughly $6d_s$), consistent with figure 11. Moreover, power-law exponents less than 0.9 suggest that $D_y : D_z$ decreases with x , indicating that the plume has encountered an upstream obstacle or undergone a transition from EP to GLP.

7 Plume type, key GDM and WSM modeling parameter

The plume type in each measurement plane is assessed by plotting z_M/z_c versus z_c/δ_{cz} , as shown in figure 14. (See §2.1, figure 1, and the accompanying discussion.) The solid black line in each subplot corresponds to the derived curve from the middle panel of figure 1, which delineates characteristic relationships for EP, GLP, and GLS plumes. The subplot layout mirrors that of figure 13; colours denote r and symbols denote P per Table 3.

For GEOM1, the plume exhibits EP behavior in the first two measurement planes and transitions to a GLP in the final plane. GEOM2 begins as an EP at the first plane, transitions to a GLP in the second (though weaker for $r \simeq 0.46$), and becomes a GLS by the third plane, largely independent of

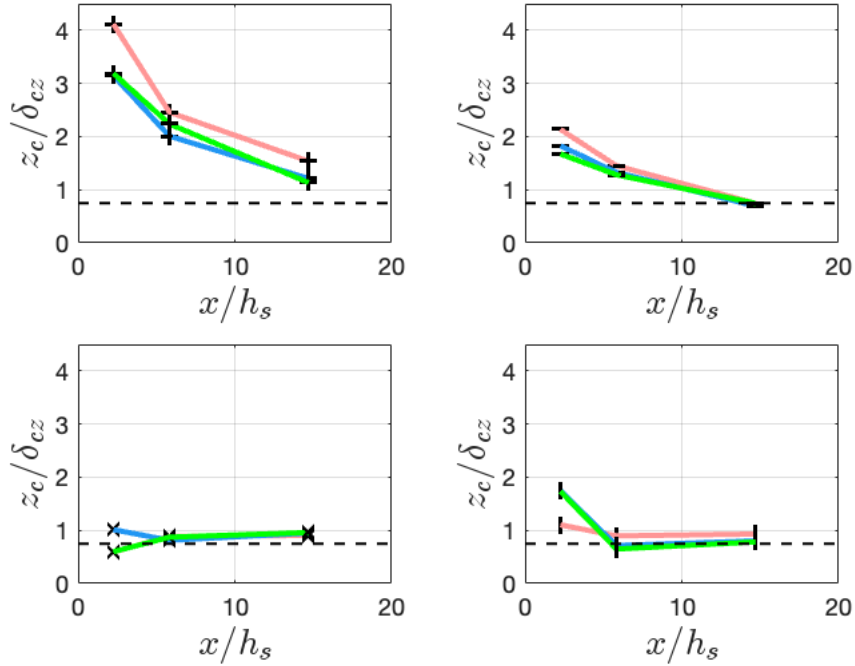


Figure 15: Normalized plume centroid z_c / δ_{cz} versus x / h_s . The figure panel layout, symbols, and line colours are identical to those in figure 13.

r . In GEOM3, the plume already resembles a GLP or near-GLS in the first plane and clearly evolves into a GLS in the subsequent planes. GEOM4 shows similar behavior, with a GLP in the first plane and a GLS in the second and third. The first measurement plane shows that GLP or near-GLS behavior observed for the low AR_1 release geometries is classified as a cavity plume, reflecting the influence of wake-induced recirculation within the obstacle's wake cavity.

The subtle differences observed between GEOM3 and GEOM4 in the first measurement plane are likely attributable to variations in the secondary aspect ratio AR_2 , which modulates the influence of wake structures on the dispersion process. Overall, the regime classifications inferred from figure 14 show good agreement with the visual plume behavior documented in figures 5–8.

The key modeling parameter for both the GDM and WSM frameworks is the streamwise evolution of the normalized plume centroid position, z_c / δ_{cz} , where z_c serves as a measurable surrogate for the effective source height, \tilde{h}_s . Figure 15 shows z_c / δ_{cz} plotted versus x / h_s . Consistent with other measures, GEOM1 and GEOM2 exhibit an r -dependence most pronounced between $r \approx 0.46$ and $r \approx 0.23$. GEOM4 shows a similar sensitivity over this r range, but with the trend reversed relative to GEOM1 and GEOM2.

The horizontal dashed line in each subplot indicates the estimated value of χ_{GLS} . As discussed in §2.2, the analytical value of χ_{GLS} depends on s and varies slightly between the GDM and WSM formulations. The rate at which the plume approaches this asymptotic GLS structure is primarily governed by the primary aspect ratio, AR_1 , with a weak dependence on r and the secondary aspect ratio AR_2 . Knowledge of $z_c / \delta_{cz} = f(x, AR_1, AR_2, r)$ provides essential, though not sufficient, information for accurately modeling low-momentum scalar releases from bluff bodies within a turbulent boundary layer.

8 Characteristics of the crosswind y -integrated profiles

The GDM crosswind y -integrated concentration profile, defined as $C'(x, z) = \int_{-\infty}^{\infty} C(x, y, z) dy$, and normalized by the peak value C'_M , is given by:

$$\frac{C'(x, z)}{C'_M} = \frac{\exp \left[-\ln(2) \frac{(z - \tilde{h}_s)^2 - (z_M - \tilde{h}_s)^2}{\delta_{cz}^2} \right] \left[1 + \exp \left(-\ln(2) \frac{4z\tilde{h}_s}{\delta_{cz}^2} \right) \right]}{1 + \exp \left(-\ln(2) \frac{4z_M\tilde{h}_s}{\delta_{cz}^2} \right)}, \quad (7)$$

where all variables are defined previously. For an EP, where $z_M = \tilde{h}_s$ and $\tilde{h}_s/\delta_{cz} > 2$, (7) simplifies to the standard Gaussian form:

$$\frac{C'(x, z)}{C'_M} = \exp \left[-\ln(2) \frac{(z - \tilde{h}_s)^2}{\delta_{cz}^2} \right]. \quad (8)$$

For a GLS, where $\tilde{h}_s/\delta_{cz} = 0$, the profile reduces to:

$$\frac{C'(x, z)}{C'_M} = \exp \left[-\ln(2) \left(\frac{z}{\delta_{cz}} \right)^2 \right]. \quad (9)$$

The WSM profile, given in (2), differs from (9) only in the value of the shape parameter s ; non-Gaussian behavior is observed when $s \neq 2$.

8.1 Assessment of GDM performance in EP–GLP–GLS regimes

Normalized crosswind y -integrated profiles C'/C'_M for GEOM1–GEOM4 (top to bottom) are shown in figure 16. Each panel includes nine profiles labeled (a–i), corresponding to combinations of velocity ratio and measurement plane: $r1P1, r1P2, r1P3, \dots, r3P3$. The velocity ratios and measurement locations are defined in Table 3, with $(r1, r2, r3) \simeq (0.46, 0.23, 0.16)$ and $(P1, P2, P3) \simeq (x = 0.64, 1.66, 4.19 \text{ m})$. The dashed lines correspond to GDM predictions obtained from (7–9), using the measured values of z_c/δ_{cz} as input.

For GEOM1, the plume transitions from an EP at $P1$ to a GLP at $P3$ for all r . The GDM provides good agreement with the data, except for profiles (f) and (i), where it overpredicts concentrations near the wall ($z/\delta_{cz} < 1$). For GEOM2, the plume descends more rapidly toward the wall than for GEOM1, with the transition occurring from EP ($P1$) to GLP ($P2$) to GLS ($P3$) as x increases. The GDM fits are consistently good across all profiles and velocity ratios. The overprediction in GEOM1 (f, i) appears to stem from cases where $z_M/\delta_{cz} < 1$, suggesting that the accuracy of the GDM is sensitive to plume behavior near the GLP–GLS transition regime. These findings suggest that the GDM effectively captures the EP–GLP–GLS transition for plumes influenced by aerodynamic downwash generated by trailing-edge vortices from the free end of the cylinder. However, it tends to overpredict wall concentrations near the GLP–GLS transition. Talluru et al. [36] likewise documented limitations of GDM predictions for point sources positioned near the wall, corresponding to a GLP–GLS transition in the present study.

For GEOM3, the plume resembles a GLS already at $P1$. The response to r is non-monotonic: $r2$ deviates more from GLS behavior than $r1$ or $r3$. By $P2$ and $P3$, the plume clearly exhibits GLS characteristics for all r . GDM fits are generally strong, with mild overprediction at $z/\delta_{cz} > 1$ for profiles (a) and (g), and moderate disagreement in (d). For GEOM4 at $P1$, the profiles remain approximately uniform from the wall out to an r -dependent distance z/δ_{cz} . This distance equals

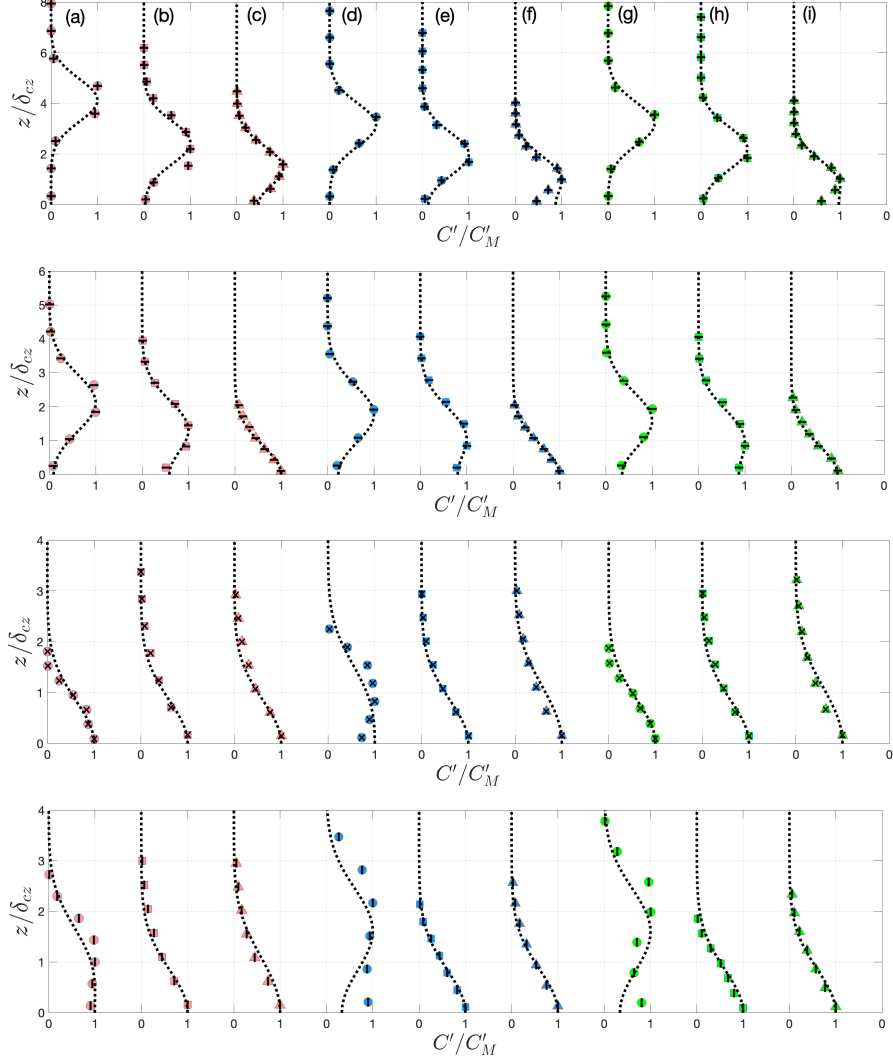


Figure 16: C'/C'_M profiles for GEOM1–GEOM4 (top-to-bottom). Each panel includes nine profiles labeled (a–i), corresponding to combinations of velocity ratio and measurement plane: $r1P1, r1P2, r1P3, \dots, r3P3$, for decreasing r and increasing P . The symbols and colours are defined in Table 3. The dashed lines denote the GDM profiles computed from (7).

h_s/δ_{cz} , indicating that C' is approximately uniform within the wake cavity. At $P2$ and $P3$, the plume fully transitions to GLS, independent of r . While the GDM performs well at $P2$ and $P3$, it underperforms at $P1$. These results indicate that while the GDM is not well-suited for capturing the EP–GLP–GLS transition in cases dominated by full-cavity entrainment (i.e., low- AR_1), it provides accurate representations of the mean vertical concentration profiles once the plume has transitioned to a GLS.

8.2 Comparison of GDM and WSM for GLS plumes

The GLS concentration profiles (see figure 16): GEOM2 panels (c), (f), and (i); GEOM3 panels (b), (c), (e), (f), (h), and (i); and GEOM4 panels (b), (c), (e), (f), (h), and (i), are replotted in figure 17. The dashed line represents the GDM prediction (9), while the solid line corresponds to WSM (2) with shape exponent $s = 1.5$.

For GEOM2, the GLS profiles are well captured by the GDM and consistently fall below the WSM prediction. In contrast, GEOM3 profiles are more accurately represented by the WSM, with some data at $z/\delta_{cz} > 2$ lying between the GDM and WSM predictions. GEOM4 profiles exhibit greater scatter at $z/\delta_{cz} > 2$, particularly for $r \simeq 0.23$ and 0.16 , although the $r \simeq 0.46$ profile aligns closely with the WSM.

A fit of the collective GLS datasets for each geometry yields optimal values of $s = 2.0$, 1.5 , and 1.7 for GEOM2, GEOM3, and GEOM4, respectively. Given the difference in normalized downstream distance (x/d_o) between GEOM3 and GEOM4, and the proximity of the GEOM2 profiles at plane $P3$ to the GLP–GLS transition, the results suggest that a finite development length beyond the GLP–GLS transition is required for GLS plumes to exhibit non-Gaussian behavior ($s < 2$).

8.3 GDM crosswind z -integrated profiles

The GDM crosswind z -integrated concentration profile, defined as $C''(x, y) = \int_{-\infty}^{\infty} C(x, y, z) dz$, and normalized by its peak value C''_M , is given by:

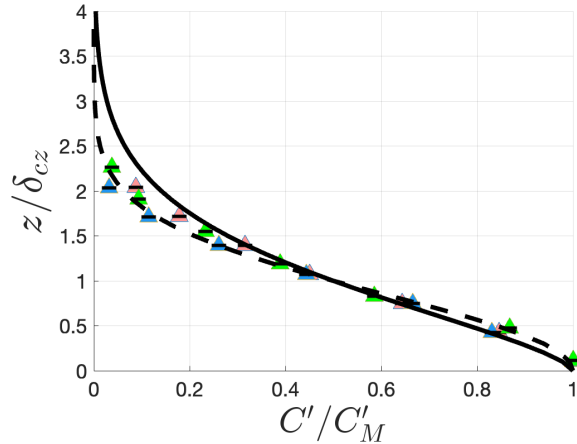
$$\frac{C''(x, y)}{C''_M} = \exp \left[-\ln(2) \frac{(y - y_s)^2}{\delta_{cy}^2} \right], \quad (10)$$

where y_s is the plume centreline position and δ_{cy} is the lateral half-width. The normalized profiles are presented in figure 18.

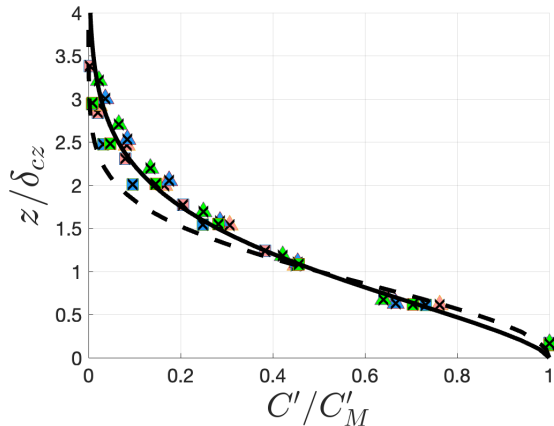
For GEOM1 and GEOM2, the lateral profiles are self-similar and well-described by a Gaussian distribution across all measurement planes and for all velocity ratios r . This Gaussian behavior supports the use of analytical solutions for modeling the mean concentration field $C'(x, z)$, while approximating lateral dispersion using the form in (10).

In contrast, the profiles for GEOM3 and GEOM4 exhibit approximate self-similarity but deviate from Gaussian behavior in some measurement planes. Notable deviations, such as reduced peak sharpness or bimodal distributions, occur at plane $P2$ and $P3$ for GEOM3 (all r), and at plane $P3$ for GEOM4 at $r \simeq 0.46$. These regions coincide with those where $\delta_{cy} \propto x^{\sim 1}$, indicating a link between enhanced lateral dispersion driven by wake structure interactions and non-Gaussian behavior.

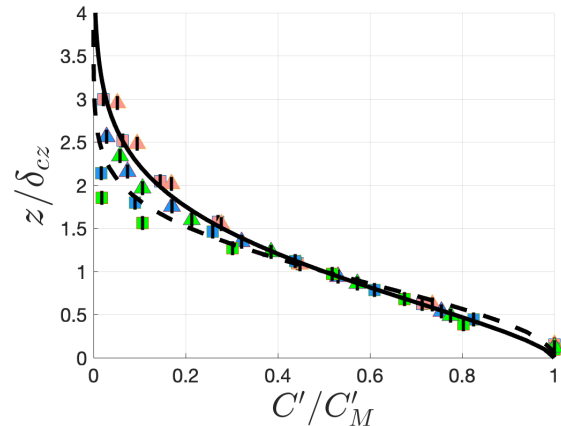
These non-Gaussian profiles for GEOM3, shown in figure 19, are well-represented by the sum of two Gaussian functions. The top row displays profiles for GEOM3 at plane $P2$, and the bottom row at plane $P3$, arranged left to right in increasing xr/d_o . At the smallest xr/d_o values ($P2$, top row), the two Gaussian peaks are centred at $y \approx \pm 0.5d_o$. As xr/d_o increases ($P3$, bottom row), the peaks



(a) GEOM2: GLS profiles



(b) GEOM3: GLS profiles



(c) GEOM4: GLS profiles

Figure 17: GLS profiles for (a) GEOM2, (b) GEOM3, and (c) GEOM4. The dashed line represents the GDM (9), while the solid line corresponds to WSM (2) with shape exponent $s = 1.5$. The symbols and colours are defined in Table 3.

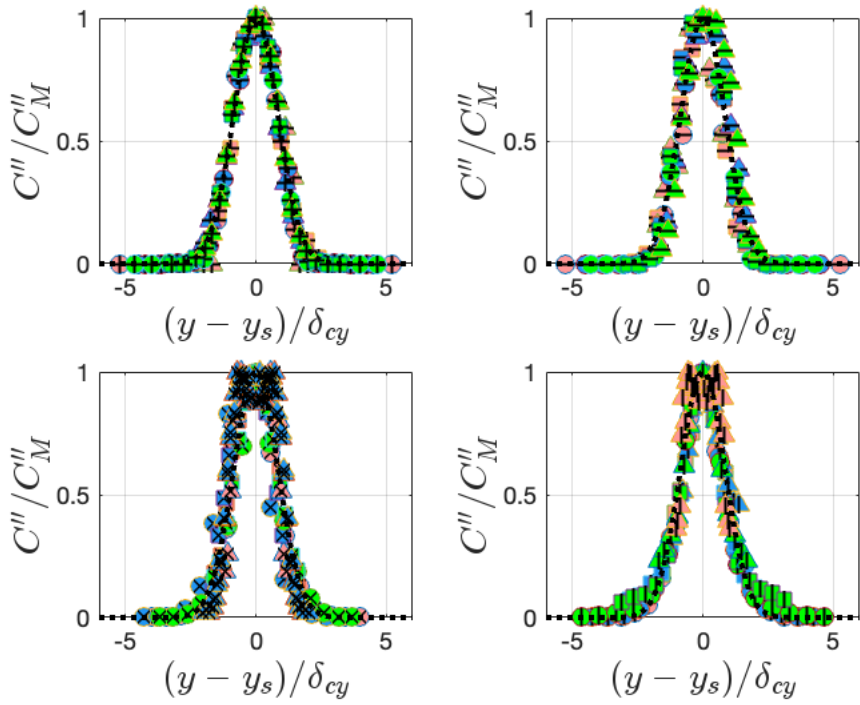


Figure 18: C''/C''_M profiles. Panels (left-to-right/top-to-bottom): GEOM1–GEOM4; colours denote r and symbols denote P per Table 3.

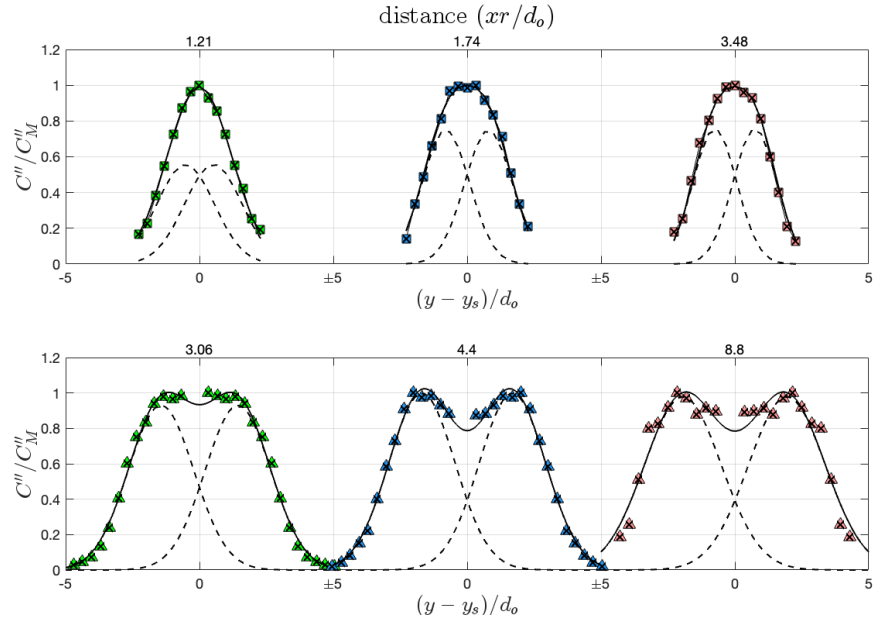


Figure 19: C''/C''_M profiles for GEOM3 at P_2 (top) and P_3 (bottom), plotted against $x/(r d_o)$. The solid curve equals the sum of two Gaussians (dashed).

spread laterally, reaching $y \approx \pm 2d_o$ by $xr/d_o \simeq 8.8$. This evolution suggests that within the wake cavity, scalar concentrations are initially trapped by the arch vortex near $\pm 0.5d_o$. As the arch vortex breaks down and tilts downstream, the horseshoe vortices disperse the concentrations laterally, producing broader lateral distributions that are well represented by the sum of two symmetric Gaussians, and are thus distinctly non-Gaussian in overall form.

As described earlier, for low- AR_1 release geometries, a plume half-width of at least $\delta_{cy}/d_o \gtrsim 0.5$ in the near-source region (i.e., within the wake cavity) appears to be a necessary condition for the arch vortex and the horseshoe vortex to significantly influence lateral spread. For GEOM4, this threshold is only reached at $r \simeq 0.46$, consistent with the observed double-peak behavior in figure 18 appearing only at $r \simeq 0.46$.

9 Data Informed Model

The measurement results obtained in this study suggest that a simplified dispersion model accounting for the effects of a bluff body on the EP–GLP–GLS transition is justified. The influence of the bluff body can be categorized into two distinct regimes:

1. plumes influenced by stack aerodynamic downwash (GEOM1 and GEOM2), and
2. plumes influenced by full cavity entrainment (GEOM3 and GEOM4).

The key geometric parameter distinguishing these two regimes is the aspect ratio AR_1 . Plumes dominated by stack aerodynamic downwash ($AR_1 \gtrsim 3$) undergo a gradual EP–GLP–GLS transition, characterized by vertical spreading and a decrease in the normalized plume centroid z_c/δ_{cz} with downstream distance x , as shown in the top row of figure 15. In contrast, plumes governed by full cavity entrainment ($AR_1 \lesssim 3$) transition rapidly from a uniform concentration profile within the cavity to a GLS.

9.1 Model Construction

Model assumptions follow directly from those used to derive the GDM. Here, $U(x)$, $D_y(x)$, and $D_z(x)$ denote the vertically averaged mean axial velocity and the effective lateral and vertical dispersion coefficients, respectively. The concentration field is assumed separable:

$$C(x, y, z) = C_y(x, y) C_z(x, z),$$

where C_y and C_z satisfy the steady-state lateral and vertical advection–diffusion equations [8, 18]. In GDM form, the transverse profiles are:

$$C_y = \exp \left[-\ln(2) \frac{(y - y_s)^2}{\delta_{cy}^2} \right] \quad (11)$$

$$C_z = \beta x^{-b} \exp \left[-\ln(2) \frac{(z - \tilde{h}_s)^2}{\delta_{cz}^2} \right] \left[1 + \exp \left(-\ln(2) \frac{4z\tilde{h}_s}{\delta_{cz}^2} \right) \right]. \quad (12)$$

As in most dispersion models, a primary goal is to predict the lateral and vertical dispersion widths $\delta_{cy}(x)$ and $\delta_{cz}(x)$. Unlike standard approaches, we additionally seek to capture the EP–GLP–GLS transition, especially when it is strongly governed by fluid–structure interactions between the release geometry and the crossflow.

9.1.1 Fitting Functions

Below is a concise introduction to our empirical fitting functions which, despite their data-driven form, often illuminate the underlying physics they represent. The detailed forms of the functions and their corresponding fit parameters are summarized in Table 6.

Peak concentration

The downwind evolution of the peak concentration is modeled using a power-law relationship:

$$\frac{C_M}{C_o} = \beta \left(\frac{x}{rd_s} \right)^{-1}, \quad (13)$$

where β is an empirical function of the aspect ratio AR_1 . Specific functional forms and fitting parameters for β are listed in Table 6.

Lateral plume half-width

A best-fit empirical power-law model for the lateral dispersion coefficient that captures the effects of AR_1 , AR_2 , and r is given by:

$$\frac{\delta_{cz}}{d_s} = C_1 \left(\frac{x}{h_s} \right)^{\gamma_1}, \quad \text{with } C_1 = \frac{j_1}{rj_2}. \quad (14)$$

Fitting parameters for j_1, j_2 and the specific functional form and fitting parameters for γ_1 are listed in Table 6

Ratio of plume centroid to vertical half-width

The downstream evolution of the normalized plume centroid, z_c/δ_{cz} , is the primary model parameter, as it governs the wall-normal centroid position and determines the streamwise locations of the EP–GLP–GLS transitions. It is modeled as:

$$\frac{z_c}{\delta_{cz}} = (1 + \Theta) \hat{z}_{c,o} \left(\frac{x}{d_o} \right)^{-\gamma_2} + \chi_{GLS}, \quad (15)$$

where $\hat{z}_{c,o} = 2\tilde{h}_s/d_s - \chi_{GLS}$ sets the initial condition (where χ_{GLS} denotes the theoretical limiting value for a GLS) and $\Theta(AR_1, AR_2, r)$ accounts for plume rise/fall in the near-source region. The exponent γ_2 is modeled as a function of AR_1 . Specific functional forms and fitting parameters for $\hat{z}_{c,o}$ and γ_2 are listed in Table 6.

9.2 Assessment of the model

The essential components of a data-driven scalar-dispersion model capable of capturing the EP–GLP–GLS transition in plumes dominated by fluid–structure interactions between release geometry and crossflow have been assembled. In this section, the model is validated against experimental data for a representative set of cases. Finally, we map the predicted ground-level concentration, C_g , across the (AR_1, AR_2, r) parameter space for low-momentum releases ($r < r_c$).

9.2.1 Crosswind y -integrated profiles

The crosswind y -integrated concentration profiles C'/C'_M are shown in figure 20. The panel arrangement matches that of figure 16. Black dashed lines show GDM predictions from (7)–(9), using the measured values of z_c/δ_{cz} as inputs, while magenta dashed lines denote model results.

Table 6: Empirical fitting functions and corresponding fit coefficients and fit parameters.

Empirical function	Fit coefficients and parameters
<i>Downwind Evolution of Peak Concentration (13)</i>	
$\frac{C_M}{C_o} = \beta \left(\frac{x}{rd_s} \right)^{-1}$	
$\beta(AR_1) = \frac{a_1}{1 + \exp[-a_2(AR_1 - a_3)]} + 0.22$	$a_1 = 0.34, a_2 = 1.68, a_3 = 5.93$
<i>Downwind evolution of lateral plume half-width (14)</i>	
$\frac{\delta_{cz}}{d_s} = C_1(x/h_s)^{\gamma_1}, \quad C_1 = \frac{b_1}{r^{b_2}}$	$b_1 = 1.88, b_2 = 1/3, \gamma_1(\alpha)$
$\gamma_1 = LL + \frac{UL - LL}{1 + \exp[(\alpha - g_1)/g_2]}$	$\alpha = \frac{AR_1}{r^{AR_2/20}}$ $LL = 0.5, UL = 1.2, g_1 = 3.1, g_2 = 0.64$
<i>Downwind evolution of ratio plume centroid to vertical half-width (15)</i>	
$\frac{z_c}{\delta_{cz}} = (1 + \Theta) \hat{z}_{co} \left(\frac{x}{d_o} \right)^{-\gamma_3} + \chi_{GLS}$	$\hat{z}_{co} = 2\tilde{h}_s/d_s - \chi_{GLS}, \Theta(\phi, R), \gamma_2(AR_1)$
$\Theta = R [\tanh(3\phi)]^3$	$\phi = \log(AR_1/AR_2)$
$\gamma_2(AR_1) = j_1 + \frac{j_2 - j_1}{1 + (AR_1/j_3)^k}$	$j_1 = 0.77, j_2 = 7.002, j_3 = 3.342, m = 6.902$
$\chi_{GLS} = B/(\ln 2)^{1/s} \approx 0.68$ for GDM,	$B(s) = \Gamma(2/s)/\Gamma(1/s), (1.5 \leq s \leq 2)$

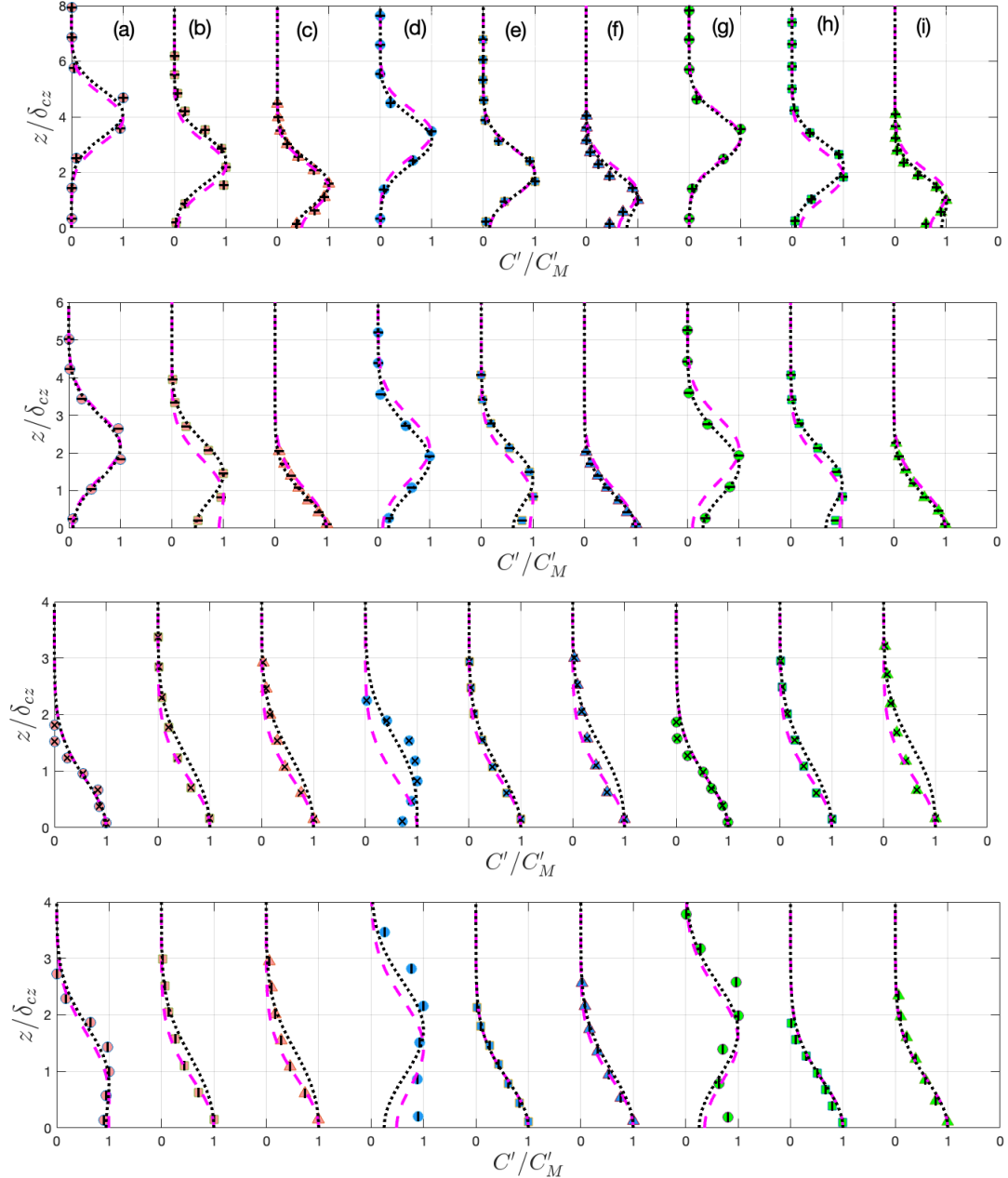


Figure 20: C'/C'_M profiles for GEOM1–GEOM4 (top-to-bottom). The panel arrangement matches that of figure 16. Black dashed denote GDM predictions using the measured values of z_c/δ_{cz} as inputs, while magenta dashed lines denote model results.

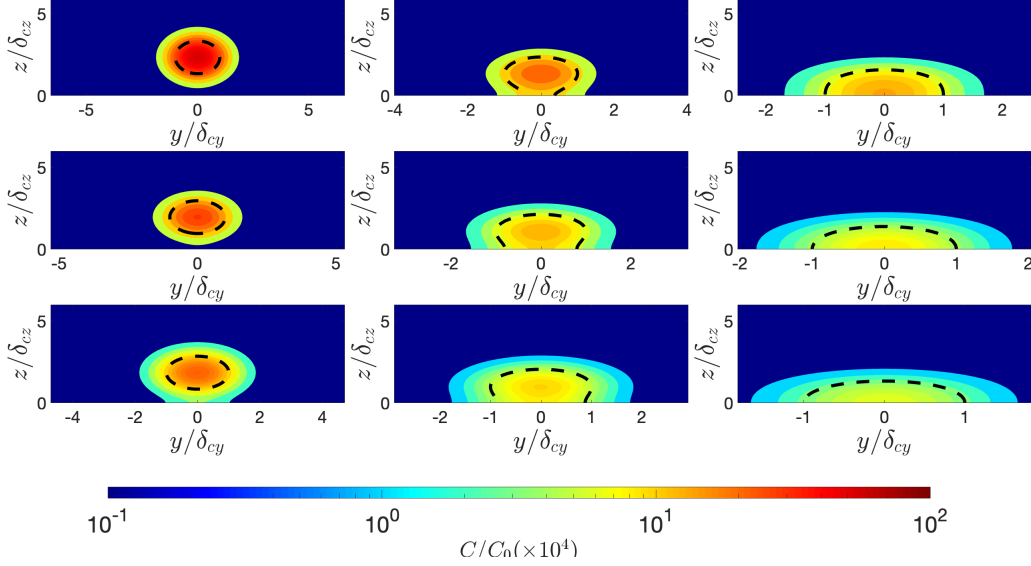


Figure 21: Modeled concentration fields of GEOM2. The panel arrangement is identical to figure 8.

Overall, the model reproduces the profiles for GEOM1 and GEOM2 with high fidelity, including the EP–GLP–GLS transition. For GEOM3 the agreement remains excellent except in profile (d) ($r2P1$), where the near-uniform concentration within the wake cavity is not captured. Similarly, for GEOM4 the agreement is excellent except for profile (d) ($r2P1$) and profile (g) ($r3P1$), where the near-uniform concentration within the wake cavity is not captured. In future work, these deficiencies for low- AR_1 geometries could be addressed by initializing the concentration field as uniform within the wake cavity.

9.2.2 Two-dimensional profiles

Planar scalar concentration fields for GEOM2 obtained from the model are presented in figure 21. The panel arrangement mirrors that of figure 8. A key distinction between figures 21 and 8 lies in the coordinate scaling: in the former, the x and y axes are dynamically scaled by δ_{cz} and δ_{cy} , respectively, while in the latter they are statically scaled by \hat{h}_s . Despite this difference, the model predictions exhibit excellent agreement with the measurements. First, the predicted concentration magnitudes closely match the observed values. Second, the model captures the enhanced lateral spread associated with the EP–GLP transition.

9.2.3 Ground-level concentration

The model is used to predict the ground-level concentration C_g at, and downstream of, the EP–GLP transition point defined by the condition $z_c/\delta_{cz} \leq 2$, across the (AR_1, AR_2, r) parameter space for low-momentum releases ($r < 1.5$). Measured and modeled C_g/C_o plotted against x/rd_o for the experimental (AR_1, AR_2, r) parameter space is shown in figure 22. The parameter r is represented by the colour map and AR_1 is distinguished by the marker shape: GEOM1 (circle), GEOM2 (square), GEOM3 (triangle), GEOM4 (diamond). Encircled markers denote measurements; unencircled markers denote modeled values.

Given that C_g/C_o requires accurate C_M , z_c/δ_{cz} , and $C(z/\delta_{cz})$ versus $x/(rd_o)$, the model performs well; right-panel errors are within ± 0.8 in C_g/C_o . The median absolute percentage error is 20%; the root-mean-square percentage error is 36%; 76% of cases fall within $\pm 50\%$ of the measurements.

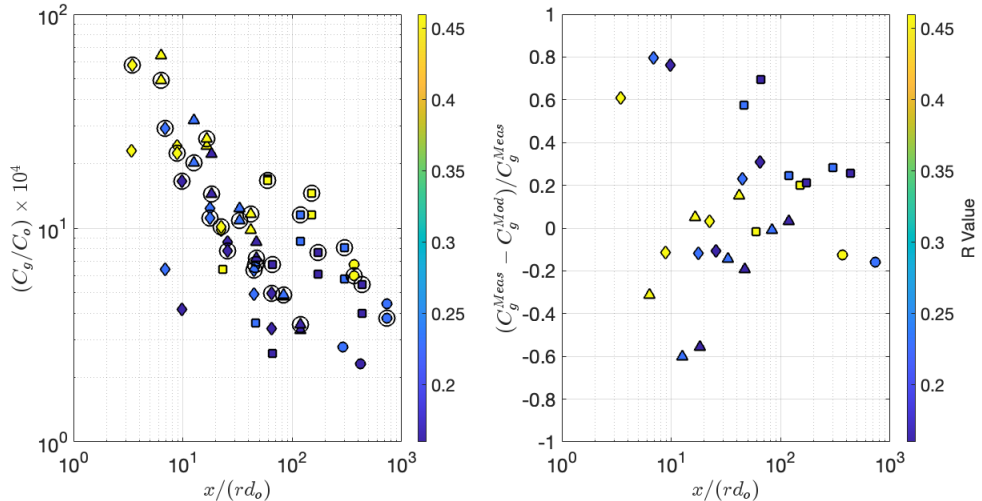


Figure 22: (left) Ground-level concentration, $(C_g/C_o) \times 10^4$ versus x/rd_o across the experimental AR_1 , AR_2 , and r parameter space. The parameter r is represented by the colour map and AR_1 is distinguished by the marker shape: GEOM1 (circle), GEOM2 (square), GEOM3 (triangle), GEOM4 (diamond). Encircled markers denote measurements; unencircled markers denote modeled values. (right) The normalized difference between the measured and modeled values of C_g/C_o .

9.3 Utility and scope of applicability

The framework yields regime-aware, data-informed predictions of ground-level concentration and profile shape from a compact set of variables, C_M and z_c/δ_{cz} , evaluated versus downwind distance x . Because the diagnostics are inexpensive and tied to observables, the method is immediately useful for rapid hazard screening, experiment design, and as validation targets for LES/RANS. For modest departures in (r, AR_1, AR_2) or obstacle details, the framework provides a sensible zeroth-order approximation. For larger departures, the formulation can be extended to include additional physics (e.g., strong buoyancy, unsteady crosswind, non-Boussinesq releases, or substantially different blockage/porosity). Importantly, the framework provides a clean initialization for WSM beyond the EP–GLP–GLS transition.

10 Conclusions

This study provides a detailed analysis of scalar dispersion from low-momentum sources released atop wall-mounted cylinders under conditions of large boundary-layer Reynolds number. By systematically varying geometric aspect ratios and the velocity ratio, we have demonstrated that plume evolution occurs through a series of well-defined transitions: from elevated plumes (EP) to ground-level plumes (GLP), and eventually to ground-level sources (GLS). These transitions are quantitatively characterized by the dimensionless parameter \tilde{h}_s/δ_{cz} , with supporting metrics such as z_c/δ_{cz} and z_M/z_c providing robust plume classification.

Our results show that the EP–GLP transition is marked by suppressed vertical growth and enhanced lateral dispersion, while the GLP–GLS transition leads to near-wall scalar accumulation and asymptotic plume flattening. The influence of aspect ratio AR_1 is dominant, particularly in determining the streamwise evolution of the plume centroid, while AR_2 introduces secondary modulation by shaping the interaction between the arch vortex and the horseshoe vortex with the

plume.

Evaluation of the Gaussian Dispersion Model (GDM) and Wall Similarity Model (WSM) against the experimental data reveals that WSM more accurately captures plume behavior in GLS regimes, especially where non-Gaussian vertical profiles emerge. However, both models exhibit limitations in transition regions, highlighting the need for new or hybrid approaches.

The comprehensive dataset presented in this study provides a valuable reference for future model development and validation, including large-eddy simulations and urban dispersion models. Building on this foundation, we developed the essential components of a data-driven scalar dispersion model capable of capturing the EP—GLP—GLS transition in plumes dominated by fluid–structure interactions between the release geometry and crossflow. The model serves as a first-order approximation for validating numerical simulations or estimating release source locations in low-momentum releases from realistic release geometries. Beyond its practical applications, this work advances our fundamental understanding of the physical mechanisms governing scalar transport in complex, wall-bounded flows with realistic release conditions.

A

A.1 Measurement uncertainty in the mean methane concentration

The uncertainty in the mean methane concentration measurements is an important consideration owing to the finite-time measurements acquired. The measurement uncertainty is evaluated from time-series data of methane concentration acquired over a ten-minute period on the centreline axis ($y/h_s = 0$) downstream of the cylinder. The ten-minute time-series data is divided into twenty time windows of thirty seconds each. The uncertainty in the mean methane concentration measurement is quantified by the standard deviation of the mean concentration computed over the twenty windows relative to the mean concentration computed over the ten-minute period [31].

For GEOM3 and GEOM4, 10-minute time-series data were acquired at

$$(x/h_s, z/h_s) : (2.24, 0.18), (2.24, 1.33), (5.82, 0.18), \text{ and } (5.82, 1.33).$$

The lower and upper z/h_s positions approximately correspond to the location of peak concentration and the upper plume edge, respectively. The measurement uncertainty for GEOM3 and GEOM4 is effectively identical. At $x/h_s = 2.24$ and $z/h_s = 0.18$ and 1.33, the measurement uncertainty in the mean concentration for a sampling period of thirty seconds at a sampling rate of 1 Hz is $\pm 6\%$ and $\pm 21\%$, respectively. At $x/h_s = 5.82$ and $z/h_s = 0.18$ and 1.33, the uncertainty is $\pm 6\%$ and $\pm 14\%$, respectively.

The identical procedure was followed for GEOM2 with 10-minute time-series data acquired at

$$(x/h_s, z/h_s) : (2.24, 0.5), (2.24, 0.8), (5.82, 0.5), \text{ and } (5.82, 0.8).$$

At $x/h_s = 2.24$ and $z/h_s = 0.5$ and 0.8, the uncertainty in the mean concentration is $\pm 5\%$ and $\pm 16\%$, respectively. At $x/h_s = 5.82$ and $z/h_s = 0.5$ and 0.8, the uncertainty is $\pm 5\%$ and $\pm 13\%$, respectively.

For GEOM1, 10-minute time-series data were acquired at

$$(x/h_s, z/h_s) : (2.24, 0.46), (2.24, 0.98), \text{ and } (2.24, 1.33).$$

The measurement uncertainty at these positions is $\pm 13\%$, $\pm 23\%$, and $\pm 40\%$, respectively. These measurement uncertainties are consistent with an analysis of the convergence of the running average

of the time-series data, but are a factor of two larger than the 95% confidence interval as quantified by the standard error of the mean for a thirty-second time window.

The measurement uncertainty is largest for GEOM1, likely because the EP regime is more intermittent than GLS [19]. The sampling time required for convergence of the mean methane concentration for GEOM1 to within 10% at $z/h_s = 0.46, 0.98$, and 1.33 is 60, 100, and 350 seconds, respectively. As discussed in §2.4, these sampling times are too long owing to the finite volume of the gas cylinder. A sampling time of thirty seconds is therefore adopted as a compromise between measurement uncertainty and the ability to acquire planar measurements of mean methane concentration. Importantly, the *Aeris Technologies MIRA Ultra LDS* operates at 1 Hz and provides volume-averaged concentration over $\approx 60 \text{ cm}^3$ via mid-infrared laser absorption spectroscopy. Thus, a 30 s sampling interval corresponds to $\approx 1,800 \text{ cm}^3$ of sampled volume.

A.1.1 Mean scalar flux

A sting-mounted pitot-static tube is used to measure mean streamwise velocity at each grid point in the planar measurement grid. The pitot-static tube is sting-mounted to the two-dimensional traverse. The pitot-static tube pressure differential is measured by a *MKS-Baratron 10 Torr* pressure transducer. The measured mean concentration and mean streamwise velocity are used to compute the mean methane mass flux downstream of the release geometry.

The mean streamwise velocity is measured either simultaneously with or independently of the methane concentration measurements. For simultaneous measurements, the methane measurement probe and pitot-static tube are offset by Δy , where Δy is the spanwise separation between grid points in the measurement grid. The pitot-tube measurements include corrections for the effects of viscosity, turbulence, velocity gradients, and the presence of the wall [14].

The uncertainty in the mean scalar flux is a combination of the uncertainty in the methane concentration measurements and the coarseness of the measurement grid. The mass flux of methane, \dot{m} , across a yz -plane at an arbitrary x position is

$$\dot{m} = \int C \rho_{CH_4} u dA, \quad (16)$$

where $C(y, z)$ is the measured volume fraction of methane computed from the *Aeris Technologies MIRA Ultra LDS*, $\rho_{CH_4}(P, T)$ is the density of methane dependent on the fluid pressure (P) and temperature (T), u is the x -component of the air velocity vector (i.e., the velocity component normal to the yz -plane) measured with a pitot-tube, and dA is an incremental area of the yz -plane.

The integrated mass flux was evaluated at $x = 1.66 \text{ m}$ and compared to the mass flux injected at the source, Q , for the four release geometries and the three freestream velocities. These twelve cases correspond to the second column in figures 5–7. The computed ratio \dot{m}/Q for twelve nine cases has a mean of 1.04, a standard deviation of 0.077, a minimum of 0.90, and a maximum of 1.18. This demonstrates that the resolution of the measurement grid and the measurement sampling time is sufficient to evaluate the methane mass flux to within $\pm 20\%$.

References

- [1] K. J. Allwine, R. N. Meroney, and J. A. Peterka. Rancho seco building wake effects on atmospheric diffusion: Simulation in a meteorological wind tunnel. Technical report, Office of Scientific and Technical Information (OSTI), February 1980. URL <https://doi.org/10.2172/5604074>.

[2] B. Blocken. LES over RANS in building simulation for outdoor and indoor applications: A foregone conclusion? *Building Simulation*, 11(5):821–870, July 2018. ISSN 1996-8744. doi: 10.1007/s12273-018-0459-3. URL <http://dx.doi.org/10.1007/s12273-018-0459-3>.

[3] S. T. Castelli and T. G. Reisin. Evaluation of the atmospheric RAMS model in an obstacle resolving configuration. *Environmental Fluid Mechanics*, 10(5):555–576, mar 2010. ISSN 1573-1510. doi: 10.1007/s10652-010-9167-y. URL <http://dx.doi.org/10.1007/s10652-010-9167-y>.

[4] G. Chochua, W. Shyy, S. Thakur, A. Brankovic, J. Lienau, L. Porter, and D. Lischinsky. A computational and experimental investigation of turbulent jet and crossflow interaction. *Numer. Heat Transf. A*, 38(6):557–572, November 2000. doi: 10.1080/104077800750021134.

[5] A. J. Cimorelli, S. G. Perry, A. Venkatram, J. C. Weil, R. J. Paine, R. B. Wilson, R. F. Lee, W. D. Peters, and R. W. Brode. AERMOD: A dispersion model for industrial source applications. Part I: General model formulation and boundary layer characterization. *Journal of Applied Meteorology*, 44(5):682–693, May 2005. ISSN 0894-8763. doi: 10.1175/jam2227.1. URL <http://dx.doi.org/10.1175/JAM2227.1>.

[6] Z. Dou, Z. Liu, L. Li, H. Zhou, and Q. Wang. Atmospheric dispersion prediction of accidental release: A review. *Emergency Management Science and Technology*, 2:9, 2022. doi: 10.48130/EMST-2022-0009.

[7] J. E. Fackrell and A. G. Robins. Concentration fluctuations and fluxes in plumes from point sources in a turbulent boundary layer. *Journal of Fluid Mechanics*, 117:1–26, April 1982. ISSN 1469-7645. doi: 10.1017/s0022112082001499. URL <http://dx.doi.org/10.1017/S0022112082001499>.

[8] E. Gavze and E. Fattal. A semi-analytical model for short-range near-ground continuous dispersion. *Boundary-Layer Meteorology*, 169(2):297–326, June 2018. ISSN 1573-1472. doi: 10.1007/s10546-018-0363-5. URL <http://dx.doi.org/10.1007/s10546-018-0363-5>.

[9] S. R. Hanna, G. A. Briggs, and Jr. Hosker, R. P. Handbook on atmospheric diffusion. Technical report, Office of Scientific and Technical Information (OSTI), January 1982. URL <https://doi.org/10.2172/5591108>.

[10] S. R. Hanna, R. J. Paine, and D. L. Southern. Comparative study of Gaussian dispersion formulas within the prairie grass project. *Journal of Applied Meteorology and Climatology*, 48 (12):2160–2177, 2009. doi: 10.1175/2009JAMC2160.1.

[11] A. Hunt and I.P. Castro. Scalar dispersion in model building wakes. *Journal of Wind Engineering and Industrial Aerodynamics*, 17(1):89–115, May 1984. ISSN 0167-6105. doi: 10.1016/0167-6105(84)90036-9. URL [http://dx.doi.org/10.1016/0167-6105\(84\)90036-9](http://dx.doi.org/10.1016/0167-6105(84)90036-9).

[12] H.D. Lim and C Vanderwel. Turbulent dispersion of a passive scalar in a smooth-wall turbulent boundary layer. *Journal of Fluid Mechanics*, 969, August 2023. ISSN 1469-7645. doi: 10.1017/jfm.2023.562. URL <http://dx.doi.org/10.1017/jfm.2023.562>.

[13] Q. Liu. Wall-mounted circular cylinder flows. *Physics of Fluids*, 36(11), November 2024. ISSN 1089-7666. doi: 10.1063/5.0237808. URL <http://dx.doi.org/10.1063/5.0237808>.

[14] B. J. McKeon, J. Li, W. Jiang, J. F. Morrison, and A. J. Smits. Pitot probe corrections in fully developed turbulent pipe flow. *Meas. Sci. Technol.*, 14:1449, 2003.

[15] R. N. Meroney. Bluff-body aerodynamics influence on transport and diffusion. *Journal of Wind Engineering and Industrial Aerodynamics*, 33(1–2):21–33, March 1990. ISSN 0167-6105. doi: 10.1016/0167-6105(90)90017-7. URL [http://dx.doi.org/10.1016/0167-6105\(90\)90017-7](http://dx.doi.org/10.1016/0167-6105(90)90017-7).

[16] Y. Miao, S. Liu, H. Zheng, Y. Zheng, B. Chen, and S. Wang. A multi-scale urban atmospheric dispersion model for emergency management. *Advances in Atmospheric Sciences*, 31(6): 1353–1365, September 2014. ISSN 1861-9533. doi: 10.1007/s00376-014-3254-9. URL <http://dx.doi.org/10.1007/s00376-014-3254-9>.

[17] Z. Mo and C-H Liu. Wind tunnel measurements of pollutant plume dispersion over hypothetical urban areas. *Building and Environment*, 132:357–366, March 2018. ISSN 0360-1323. doi: 10.1016/j.buildenv.2018.01.046. URL <http://dx.doi.org/10.1016/j.buildenv.2018.01.046>.

[18] F. T. M. Nieuwstadt. Application of mixed-layer similarity to the observed dispersion from a ground-level source. *Journal of Applied Meteorology*, 19(2):157–162, 1980. doi: 10.1175/1520-0450(1980)019<0157:AOMLST>2.0.CO;2.

[19] C. Nironi, P. Salizzoni, M. Marro, P. Mejean, N. Grosjean, and L. Soulhac. Dispersion of a passive scalar fluctuating plume in a turbulent boundary layer. Part I: Velocity and concentration measurements. *Boundary-Layer Meteorology*, 156(3):415–446, May 2015. ISSN 1573-1472. doi: 10.1007/s10546-015-0040-x. URL <http://dx.doi.org/10.1007/s10546-015-0040-x>.

[20] G. Palau-Salvador, T. Stoesser, J. Fröhlich, M. Kappler, and W. Rodi. Large eddy simulations and experiments of flow around finite-height cylinders. *Flow, Turbulence and Combustion*, 84(2):239–275, August 2009. ISSN 1573-1987. doi: 10.1007/s10494-009-9232-0. URL <http://dx.doi.org/10.1007/s10494-009-9232-0>.

[21] F. Pasquill. *Atmospheric diffusion*. Ellis Horwood Ltd, Publisher, Harlow, England, 2 edition, January 1974.

[22] R. J. Pattenden, S. R. Turnock, and X. Zhang. Measurements of the flow over a low-aspect-ratio cylinder mounted on a ground plane. *Experiments in Fluids*, 39(1):10–21, May 2005. ISSN 1432-1114. doi: 10.1007/s00348-005-0949-9. URL <http://dx.doi.org/10.1007/s00348-005-0949-9>.

[23] H. Rinoshika, A. Rinoshika, Jin-Jun Wang, and Y. Zheng. 3D flow structures behind a wall-mounted short cylinder. *Ocean Engineering*, 221:108535, February 2021. ISSN 0029-8018. doi: 10.1016/j.oceaneng.2020.108535. URL <http://dx.doi.org/10.1016/j.oceaneng.2020.108535>.

[24] A.G. Robins. Plume dispersion from ground level sources in simulated atmospheric boundary layers. *Atmospheric Environment (1967)*, 12(5):1033–1044, January 1978. ISSN 0004-6981. doi: 10.1016/0004-6981(78)90348-7. URL [http://dx.doi.org/10.1016/0004-6981\(78\)90348-7](http://dx.doi.org/10.1016/0004-6981(78)90348-7).

[25] E. Robson, R. On the theory of plume trapping by an elevated inversion. *Atmospheric Environment*, 17(10):1923–1930, 1983. doi: 10.1016/0004-6981(83)90350-5.

[26] R. Rossi and G. Iaccarino. Numerical simulation of scalar dispersion downstream of a square obstacle using gradient-transport type models. *Atmospheric Environment*, 43:2518–2531, 2009.

[27] N. Rostamy, D. Sumner, D.J. Bergstrom, and J.D. Bugg. Local flow field of a surface-mounted finite circular cylinder. *Journal of Fluids and Structures*, 34:105–122, October 2012. ISSN

0889-9746. doi: 10.1016/j.jfluidstructs.2012.04.014. URL <http://dx.doi.org/10.1016/j.jfluidstructs.2012.04.014>.

[28] K. Sada and A. Sato. Numerical calculation of flow and stack-gas concentration fluctuation around a cubical building. *Atmospheric Environment*, 36(35):5527–5534, November 2002. ISSN 1352-2310. doi: 10.1016/s1352-2310(02)00668-4. URL [http://dx.doi.org/10.1016/S1352-2310\(02\)00668-4](http://dx.doi.org/10.1016/S1352-2310(02)00668-4).

[29] L. L. Schulman, D. G. Strimaitis, and J. S. Scire. Development and evaluation of the PRIME plume rise and building downwash model. *Journal of the Air & Waste Management Association*, 50(3):378–390, mar 2000. ISSN 2162-2906. doi: 10.1080/10473289.2000.10464017. URL <http://dx.doi.org/10.1080/10473289.2000.10464017>.

[30] R.F. Shi, G.X. Cui, Z.S. Wang, C.X. Xu, and Z.S. Zhang. Large eddy simulation of wind field and plume dispersion in building array. *Atmospheric Environment*, 42(6):1083–1097, February 2008. ISSN 1352-2310. doi: 10.1016/j.atmosenv.2007.10.071. URL <http://dx.doi.org/10.1016/j.atmosenv.2007.10.071>.

[31] Y. Shirian, J. A. K. Horwitz, and A. Mani. On the convergence of statistics in simulations of stationary incompressible turbulent flows. *Computers & Fluids*, 266:106046, 2023. doi: 10.1016/j.compfluid.2023.106046.

[32] S. H. Smith and M.G. Mungal. Mixing, structure and scaling of the jet in crossflow. *J. Fluid Mech*, 357:83–122, 1998.

[33] D. Sofia, N. Lotrecchiano, A. Giuliano, D. Barletta, and M. Poletto. Pollution dispersion from a fire using a Gaussian plume model. *Environmental Science & Technology*, 54(24):15622–15631, 2020. doi: 10.1021/acs.est.0c04986.

[34] D. Sumner. Flow above the free end of a surface-mounted finite-height circular cylinder: A review. *Journal of Fluids and Structures*, 43:41–63, November 2013. ISSN 0889-9746. doi: 10.1016/j.jfluidstructs.2013.08.007. URL <http://dx.doi.org/10.1016/j.jfluidstructs.2013.08.007>.

[35] D. Sumner, J. L. Heseltine, and O. J. P. Dansereau. Wake structure of a finite circular cylinder of small aspect ratio. *Experiments in Fluids*, 37(5):720–730, September 2004. ISSN 1432-1114. doi: 10.1007/s00348-004-0862-7. URL <http://dx.doi.org/10.1007/s00348-004-0862-7>.

[36] K. M. Talluru, C. Hernandez-Silva, J. Philip, and K. A. Chauhan. Measurements of scalar released from point sources in a turbulent boundary layer. *Measurement Science and Technology*, 28(5):055801, March 2017. ISSN 1361-6501. doi: 10.1088/1361-6501/aa614a. URL <http://dx.doi.org/10.1088/1361-6501/aa614a>.

[37] R. S. Thompson. Building amplification factors for sources near buildings: A wind-tunnel study. *Atmospheric Environment. Part A. General Topics*, 27(15):2313–2325, October 1993. ISSN 0960-1686. doi: 10.1016/0960-1686(93)90400-s. URL [http://dx.doi.org/10.1016/0960-1686\(93\)90400-s](http://dx.doi.org/10.1016/0960-1686(93)90400-s).

[38] Y-H Tseng, C. Meneveau, and M. B. Parlange. Modeling flow around bluff bodies and predicting urban dispersion using large eddy simulation. *Environmental Science & Technology*, 40(8): 2653–2662, March 2006. ISSN 1520-5851. doi: 10.1021/es051708m. URL <http://dx.doi.org/10.1021/es051708m>.

- [39] A. P. van Ulden. Simple estimates for vertical diffusion from sources near the ground. *Atmospheric Environment* (1967), 12(11):2125–2129, January 1978. ISSN 0004-6981. doi: 10.1016/0004-6981(78)90167-1. URL <https://www.sciencedirect.com/science/article/pii/0004698178901671>.
- [40] Wm. J. Veigle and J. H. Head. Derivation of the Gaussian plume model. *Journal of the Air Pollution Control Association*, 28(11):1139–1140, November 1978. ISSN 0002-2470. doi: 10.1080/00022470.1978.10470720. URL <http://dx.doi.org/10.1080/00022470.1978.10470720>.
- [41] P. Vincenti, J. Klewicki, C. Morrill-Winter, C. White, and M. Wosnik. Streamwise velocity statistics in turbulent boundary layers that spatially develop to high Reynolds number. *Expts. Fluids*, 54:1629, 2013.
- [42] Z-T Xie and I. P. Castro. Large-eddy simulation for flow and dispersion in urban streets. *Atmospheric Environment*, 43(13):2174–2185, April 2009. ISSN 1352-2310. doi: 10.1016/j.atmosenv.2009.01.016. URL <http://dx.doi.org/10.1016/j.atmosenv.2009.01.016>.